From solar wind to blazars: Analyzing time series with horizontal visibility graphs

Thesis
submitted to the
University Of Chile
in partial fulfillment of the requirements
for the degree of
Master of Sciences with mention in Physics
Faculty of Sciences

by

Belén Ayleen Acosta Azócar

October, 2022

Thesis Advisors: **Dr. Pablo S. Moya**
Dr. Denisse Pastén
Dr. Walter Max-Moerbeck

FACULTY OF SCIENCES

UNIVERSITY OF CHILE

APPROVAL REPORT

MASTER THESIS

The Graduate School of the Faculty of Sciences is informed that the Master's Thesis presented by the candidate

Belén Ayleen Acosta Azócar

has been approved by the Thesis Evaluation Committee as a requirement for the Master's degree, in the Private Thesis Defense examination given on December 19, 2022.

Thesis Advisors

Dr. Pablo Moya _____

Dr. Denisse Pastén _____

Thesis Co-Advisor

Dr. Walter Max-Moerbeck _____

Thesis Evaluation Committee

Dr. Víctor Muñoz _____

Dr. Paulina Lira _____

Dr. Mario Riquelme _____

Biography

Belén Ayleen Acosta Azócar was born in Santiago on August 14, 1996. She is the middle daughter of her parents Bernarda and Andrés. Belén is younger sister of Nicolás and older sister of Sofía, the best of two worlds. She is the granddaughter of Mercedes Tripailao Huera, who taught her the Mapuche cosmovision and also cared for her during her childhood. Since she was a child, she showed a certain logical-mathematical interest. Her fascination for science began during her school education. She enjoyed the subjects of Mathematics and Language. So when the time came to learn Physics, everything took on the meaning that she was looking for. Solving problems through mathematical formalism and listening to her teacher talk about astronomy confirmed her desire to be a scientist.

In 2015 she entered the Pontifical Catholic University of Valparaíso to study Bachelor's degree in Physics, where she reaffirmed her academic interests. After the first year, she continued her career in the Faculty of Sciences at the University of Chile, facing constant new challenges. She began her graduate studies in 2020 at the same University, carrying out her Master in Sciences with mention in Physics through this thesis.

Acknowledgments

I would like to thank my advisors for guiding me on the journey to be a scientist. I thank those who have given me their love and support in every challenge I have decided to face.

This thesis and my stay in this Master was funded by ANID Chile through FONDECYT grant N° 1191351 *"Kinetic instabilities and wave-particle interactions in non Maxwellian plasmas. Linear, quasi-linear, and non-linear analysis"* (Principal Investigator: Dr. Pablo S. Moya).

This thesis has made use of data from the Wind mission (NASA CDAWeb), World Data Center SILSO, and the OVRO 40-m monitoring program. The latter has been supported by private funding from the California Institute of Technology and the Max Planck Institute for Radio Astronomy, and by NASA grants NNX08AW31G, NNX11A043G, and NNX14AQ89G and NSF grants AST-0808050 and AST- 1109911.

Table of Contents

Abstract

In the case of astronomical observations, it is useful to work with new methods that are effective to complement the characterization of systems for which only limited information is available. The generality of the *Horizontal Visibility Graph* method on time series allows us to cover two systems of interest in this thesis: solar wind and blazars. The solar wind corresponds to the continuation of the solar corona where its plasma expands in space with velocities between $\approx$ 250–800 $\mathrm{km\,s^{-1}}$. On the other hand, blazars are a type of active galactic nuclei that are very luminous and variable throughout the electromagnetic spectrum. First, we tested the algorithm on *Particle In Cell* simulations of magnetized plasma. Second, we worked on solar wind magnetic fluctuations using Wind satellite measurements. Third, we worked on blazar light curves, to characterize different sources monitored with the OVRO 40m telescope in the 15 GHz radio band. We model the information presented in time series for each object of study as a complex network in the search for a new study perspective for astrophysical systems. The goal is to explore their variability and dissipative characteristics by obtaining the *Kullback-Leibler Divergence*, a measure of the degree of irreversibility between directed degree distributions, and the *critical exponent* of the undirected degree distribution, a measure that recognizes between correlated stochastic and uncorrelated chaotic time series. In the case of plasma simulations, both complexity parameters are related to the shape of the velocity distribution function. The *Kullback-Leibler Divergence* proves to be sensitive enough to detect differences between the slow and fast solar wind, while the *critical exponent* could play a role in distinguishing between spectral classes of blazars.

Resumen

Frente a observaciones astronómicas resulta útil trabajar con nuevos métodos que sean efectivos para complementar la caracterización de sistemas de los que sólo se cuenta con información reducida. La generalidad del método *Horizontal Visibility Graph* sobre series de tiempo nos permite abarcar dos sistemas de interés en esta tesis: viento solar y blazares. El viento solar corresponde a la continuación de la corona solar donde su plasma se expande en el espacio con velocidades entre ≈ 250–$800\,\mathrm{km\,s^{-1}}$. Por otro lado, los blazares son un tipo de núcleos galácticos activos muy luminosos y variables en todo el espectro electromagnético. Primero, probamos el algoritmo en simulaciones *Particle in Cell* de plasma magnetizado. Segundo, trabajamos sobre fluctuaciones magnéticas de viento solar utilizando las mediciones del satélite Wind. Y tercero, sobre las curvas de luz de blazares, para caracterizar distintas fuentes monitoreadas con el telescopio OVRO 40m en la banda de radio a 15 GHz. Modelamos la información presentada en series de tiempo de cada objeto de estudio como una red compleja en la búsqueda de una nueva perspectiva de estudio para sistemas astrofísicos. El objetivo es explorar en torno a su variabilidad y sus características disipativas a partir de la obtención de la *Divergencia Kullback-Leibler*, una medida de la irreversibilidad entre las distribuciones de grado de la red dirigida, y del *exponente crítico* de la distribución de grado de la red no dirigida, una medida que reconoce entre series de tiempo estocásticas correlacionadas y caóticas no correlacionadas. Ambos parámetros de complejidad están relacionados con la distribución de la velocidad de las simulaciones de plasma. La *Divergencia Kullback-Leibler* demuestra ser lo suficientemente sensible como para detectar diferencias entre el viento solar lento y el rápido. Mientras, el *exponente crítico* podría tener un rol en la distinción de las subclases de blazares.

Chapter 1

Introduction

Graph theory seeks to schematically extract data sets employing specific geometrical criteria based on nodes or vertices and some kind of relationship with other nodes through edges, where these nodes can have a defined orientation, with a source node and a destination node. This theory was introduced in 1736 by Leonhard Euler, in an article that dealt with the problem known as the bridges of Königsberg [1] whose initial purpose was to determine the route across all the bridges of the city with the restriction of crossing them only once. Euler proved the impossibility of the case. However, this milestone prompted the development of important studies, allowing since then great advances in several areas, such as urban planning [2], economics [3], biological networks [4], and even in the selection of fundamental approaches in health, such as the spread of diseases [5], delivering substantial solutions to complex problems.

Complex networks are a powerful tool to study physical phenomena in a wide variety of systems and topics from a different perspective than usual approaches [6]. Depending on the characteristics sought to be explored in each research, there are different types of graphs and representation structures to work with. In the analysis of the data relevant to this thesis, we are interested in modeling time series as complex

networks. For this purpose, we have the tools of the family of visibility algorithms that convert time series into graphs, where the structure of the series, in terms of its temporal ordering and magnitude of the data, is preserved in the topology of the graph [7], managing to build a natural bridge between the theory of complex networks and time series analysis. The method of Visibility Graph [8] has been developed in the last years, it allows us to study and analyze time series avoiding tedious and the high computational cost that other methods offer. With this algorithm, each data in the series corresponds to a node, and two nodes are connected if there is oblique visibility between the height of the data (height determined by their magnitude). The Visibility Graph method develops a simple and direct time series analysis in self-organized critical phenomena, such as macroeconomic systems [9], biological systems [10], seismicity [11], or space plasmas [12–14].

Within the Visibility Graph algorithm, there is a simplification: the Horizontal Visibility Graph (HVG), proposed by Luque et al. [15]. In this case, the nodes are connected if it is possible to draw a horizontal line between them. This method assigns a network to a time series according to a geometric criterion that considers the magnitude of the data and its horizontal visibility with others. From the degree distributions of the complex network, Lacasa and Toral [16] associated a characteristic exponent γ with the nature of the correlations dominating time series, and Lacasa et al. [17] measured the irreversibility of real-valued time series with the Kullback-Leibler Divergence (KLD). So far, the HVG has been applied to different systems, from earthquakes [18] and plasmas [19] to chaotic processes [16]. It has been demonstrated that the method is computationally efficient since it correctly distinguishes between reversible and irreversible stationary time series. This analysis was based on analytical and numerical studies for reversible stochastic processes

(uncorrelated and linearly correlated Gaussian), irreversible stochastic processes (a discrete intermittent ratchet in asymmetric potential), reversible (conservative) and irreversible (dissipative) chaotic maps and dissipative chaotic maps in the presence of noise [17]. The KLD is sensitive to non-evident characteristics of time series [20], being an indicative feature of the presence of nonlinearities in the time series produced by the underlying dynamics associated with non-equilibrium systems in the field of thermodynamics [21]. The latter contributes to obtaining an approach to the entropy production from the time series generated by the physical system, where a high degree of irreversibility is related to a dissipative system.

Various missions are providing a wide range of time series data to understand important astrophysical phenomena that challenge us to implement new methods that are effective in complementing the characterization of this constantly new information and, sometimes, extremely reduced especially when dealing with observational data with intermittent gaps. The methodology of this thesis uses the directed and undirected versions of HVG to obtain degree distributions in both cases. It leads us to explore the dissipative characteristics of the time series by obtaining the γ-exponent, a measure proposed as a degree of stochasticity of the undirected network, and the KLD, a measure of the degree of irreversibility of the directed network. This last complexity parameter is known under various names, including the Kullback–Leibler distance, cross-entropy, information divergence, and information for discrimination [22]. Meanwhile, stochastic processes also play a fundamental role in many scientific fields where we can find dynamics in a collection of random variables evolving [23]. The advantage of KLD is that unlike other measures used to estimate irreversibility over time, KLD is statistically significant, as demonstrated by the Chernoff–Stein lemma [17]. Moreover, in the case of astronomical observations, it is

common for the data measured by telescopes to be contaminated by atmospheric (reversible) noise, yet irreversible signals continue to be well characterized by the HVG method and the KLD measurement [17].

Among the first approaches to astrophysical systems through the use of horizontal visibility graphs, Suyal et al. [19] worked on the solar wind, a turbulent plasma whose variations in terms of velocity, proton density, temperature, and helium content lead to evolving dynamical phenomena throughout the heliosphere on various temporal and spatial scales [24]. Today it is already known that the solar wind has a three-dimensional structure that varies along with the 11-year solar cycle [25], that some complexity parameters such as entropy [26], Lyapunov exponent [27], and correlation dimension [28], show that solar wind velocity fluctuations are a consequence of complex nonlinear dynamical processes.

It is not only the analysis of electromagnetic effects in the solar wind plasma that has been an area of considerable research interest in recent years. While the solar wind is the best-studied system as one of the closest astrophysical plasma laboratories to Earth, the study of blazars is another area of interest with an ever increasing amount of data available. In this thesis, we are extending the application of a novel methodology to a particular type of Active Galactic Nuclei (AGN), blazars, to characterize their high-energy emission mechanisms by analyzing the variability of the light curves of more than a thousand sources. Emission within an AGN is produced by the accretion of matter by a black hole at its center, where the surrounding material forms an accretion disk that is heated by the dissipation of gravitational energy, generating, in some cases, the expulsion of matter and energy in relativistic jets [29]. Blazars are fascinating AGN, as they are characterized by a very luminous and rapidly varying continuum emission at all observed frequencies, from radio to

gamma-rays [30], with a jet oriented close to our line of sight.

Here, we apply the HVG method to study time series in two different astrophysical contexts of great interest: solar wind and blazars. Specifically, we work with the magnetic field fluctuations associated with the solar wind, whose data are obtained from the Wind mission, where we look for correlations between the classification of the fast and slow solar wind at 1 AU during solar cycles 23 and 24, with the degree of irreversibility and stochasticity of the time series, being able to relate with the region of origin of emission of the expanding plasma. For this purpose, we first apply the method on time series of magnetic field fluctuations obtained from Particle In Cell (PIC) simulations of a non-collisional magnetized plasma. We plan to validate the technique by mastering parameters of particle velocity distributions considering the well-known kappa-distributions [31] along with the Maxwell-Boltzmann distribution, i.e., non-thermal and thermal distributions respectively, to assess whether there is any relationship with the KLD. Because solar wind is a well-described system, we aim to learn what the results of applying HVG to this system mean physically. Then, based on what we have learned in the study of the solar wind with HVG, we can extend this knowledge to the study of blazars observed with a large-scale, fast cadence 15 GHz radio monitoring program with the Owens Valley Radio Observatory (OVRO) 40 m Telescope. In the latter, we seek to describe the light curves of the sources, i.e., to analyze the observed flux density as a function of time as a first approximation of the complexity parameters in AGN. We propose to analyze which physical properties could be conditioning the behavior of the light curves, behavior that could be represented in the parameters of the complex network extracted from these time series, to find possible correlations with their spectral classification and luminosity [32, 33].

Faced with the underlying phenomenology in the data series for these two astrophysical systems, essentially due to the effect of their magnetohydrodynamic activity, the main question to answer is: What dissipative characteristics can we associate with each system from the information provided by a time series?

This thesis is organized in three main parts. In Chapter 2, the HVG method is introduced, and it defines how the stochasticity degree and the KLD value of the complex network are obtained. In the three following chapters, the application of the method in PIC plasma simulations (Chapter 3), solar wind (Chapter 4), and blazars (Chapter 5) is displayed. Each chapter includes the bibliographical antecedents necessary to go deeper into each system, the context of their most used methodologies, a description of the available time series, and the results obtained. These results are discussed in Chapter 6 individually, to finally conclude what we have learned by analyzing the time series with horizontal visibility graphs in these different contexts.

Chapter 2

Mapping time series to networks

Our study aims to interweave the key aspects driving the topology of complex networks with the physical mechanisms responsible for the variability of the time series. It is essential to study the topology of the interactions between the components, i.e., the networks through the connections between the nodes [34]. Tools and measures need to be applied to quantitatively assess the principles that organize the information in the time series. The tools of complex networks offer a different approach to describe this non-trivial interconnected information. With the visibility algorithms, these connections are related to the variability and the succession of events over time.

The visibility algorithm proceeds to map a times series into a complex network under a geometric principle of visibility. In this sense, the algorithm could be considered as a geometric transformation of the time series in which this method decomposes a time series in connections between nodes that could be repeated or not, forming a particular weave that represents the time series as a topological object. The visibility graph is constructed under a visibility criterion. Within the time series, two data (t_a, y_a) and (t_b, y_b) see each other if there is another data (t_c, y_c), with $t_a < t_c < t_b$,

such that it satisfies the condition [8, 17]:

$$y_c < y_a + (y_b - y_a)\frac{t_c - t_a}{t_b - t_a}\,. \tag{2.1}$$

Thus, this condition must be evaluated on all data. This implies oblique visibility between nodes. In this chapter, we detail the method that gives basis to this thesis, which consists of a simplification of the principle of the visibility graph in the sense that a horizontal visibility criterion will be considered from nodes (connections arise from the heights of the data, determined by their magnitude). The HVG method brings parameters that characterize the time series, the critical exponent γ, and the Kullback-Leibler Divergence D. Here, we describe in full detail the derivation of these complexity parameters, which are relevant to our purpose of characterizing the astrophysical systems under study.

2.1. Horizontal Visibility Graph

The HVG method allows the study of dynamic systems through the characterization of their networks associated with the time series [35]. As we can see in Figure 2.1, the HVG algorithm consists first of assigning a node to each data in the time series. Then, depending on the magnitude of the data, the node acquires horizontal visibility with other nodes. Thus two nodes i and j in the graph are connected if one can draw a horizontal line in the time series joining x_i and x_j that does not intersect any intermediate data height.

For directed Horizontal Visibility Graph (DHVG), first let $\{x_i\}_{i=1,\ldots,n}$ be a time series of n data. The algorithm consists of assigning each data of the series to a node. Then, for outgoing connections, i is a node that will always be connected with its

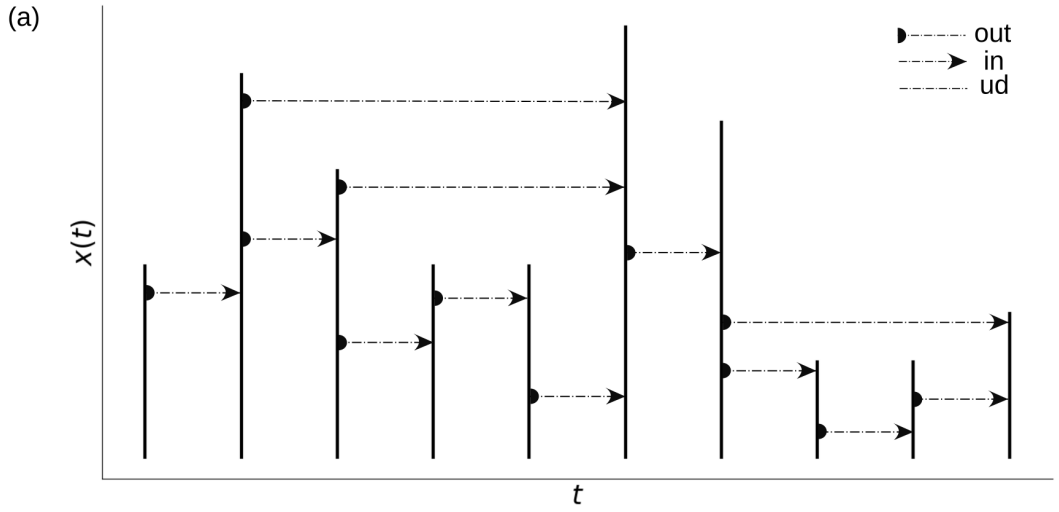

(b)

k_{out}	1	2	2	1	1	1	2	1	1	0
k_{in}	0	1	1	1	1	3	1	1	1	2
k_{ud}	1	3	3	2	2	4	3	2	2	2

Figure 2.1: (**a**) A graphical description for modeling a time series with a horizontal visibility graph. Each data correspond to a node. (**b**) According to the visibility of each node, we can calculate the degrees k_{in} and k_{out} for directed HVG and k_{ud} for undirected HVG: that is, how many connections the node establishes in function, and independently, of the temporal direction.

consecutive node $i+1$, and it will be connected to other future nodes j if

$$x_i,\ x_j > x_m \quad \forall\, m:\ i < m < j\,,\ \text{with}\ j > i+1\,, \tag{2.2}$$

and it is fulfilled within the time series for all the data that compose it [15]. Now in reverse order, for ingoing connections, i is a node that will always be connected with its previous node $i-1$, and it will be connected to other past nodes j if

$$x_i,\ x_j > x_m \quad \forall\, m:\ i > m > j\,,\ \text{with}\ j < i-1\,. \tag{2.3}$$

The presence of a data magnitude greater than or equal to the data under study interrupts its visibility. Once all the links are established for the i node, each node will have degrees denoted k_{out} and k_{in} for outgoing and ingoing connections, respectively,

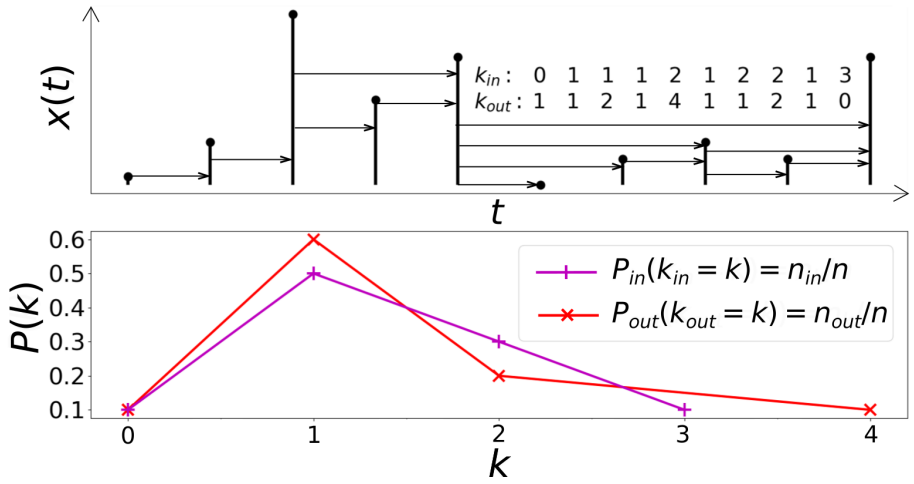

Figure 2.2: Construction of Horizontal Visibility Graph. Top, a time series where the degree k_{in} for in-going links and k_{out} for out-going links of each of the $n = 10$ nodes are detailed. Bottom, probability distribution P as a function of degree k, where n_{in} and n_{out} correspond to the frequency of appearance of the degrees k_{in} and k_{out} respectively, defining P_{in} and P_{out}.

based on the number of times the condition 2.2 is satisfied in the time direction, and 2.3 in the inverse time direction. Then, within a graph directed in the direction of the time axis, for a given node two different degrees are distinguished. These are the in-going degree k_{in}, related to how many nodes see a given node i, and an out-going degree k_{out} that is the number of nodes that node i sees [15]. With this temporal direction, the in-going degree k_{in} is associated with links of a node with other nodes of the past. Meanwhile, the degree of output k_{out} is associated with the links with nodes of the future [17]. From the properties of these connections, it can be said that if the graph remains invariant under the reversion of time, it could be stated that the process that generated the series is conservative [15]. With the already constructed DHVG, we can extract the undirected version (UHVG) considering a total degree as the sum of both: $k_{\text{ud}} = k_{\text{in}} + k_{\text{out}}$.

To further detail the dynamics between nodes or how interconnected information is related, degree distributions play a fundamental role. The degree distribution of a graph describes the probability of an arbitrary node to have degree k (i.e. k links) [36]. Thus, by counting the frequency of occurrence of each degree, we obtain degree distributions or probability distributions in the form $P(k) = n_k/n$, where n is the number of data points in the time series and n_k is the number of nodes having degree k. Namely, $P = P(k_{\text{ud}})$ for UHVG, $P_{\text{in}} = P(k_{\text{in}})$ and $P_{\text{out}} = P(k_{\text{out}})$ for DHVG. See Figure 2.2 for a graphical illustration of directed degree distributions.

2.2. Characteristic exponent γ

According to a theorem for uncorrelated time series [15], the degree distribution for the UHVG associated with a bi-infinite sequence of independent and identically distributed random variables extracted from a continuous probability density, have an exponential behavior of the form $P(k) = \frac{1}{3}\left(\frac{2}{3}\right)^{k-2}$ [15]. This can be rewritten as

$$P(k) \sim \exp\left(-\gamma_{un} k\right), \tag{2.4}$$

with $\gamma_{\text{un}} = \ln(3/2) \approx 0.405$, that is a limit for the uncorrelated situation proposed by Lacasa and Toral [16] to discriminate between correlated stochastic ($\gamma > \gamma_{\text{un}}$), or chaotic ($\gamma < \gamma_{\text{un}}$) processes. Here, γ is the characteristic exponent (the γ-exponent) of the degree distribution modeled as $P(k) \sim \exp(-\gamma k)$. In this sense, the probability distribution of the undirected degrees gives information related to the correlations in a process, in this case, time correlations. The value for γ_{un} was supported by analytical developments that confirmed the results provided by numerical simulations and experimental time series, but new studies show there are certain exceptions to this rule to take in consideration. Ravetti et al. [37], Zhang et al. [38] studied in

depth the methodology proposed by Lacasa and Toral [16] and found several cases in which their hypothesis is not valid.

The choice of the domain for the fitted straight line of the logarithm of the probability distribution is very delicate. Ravetti et al. [37] found that sometimes, non-exponential behaviors occur, and the heavy tail of the degree distribution makes the method dependent on additional adjustments on a case-by-case basis. However, the gamma value gives useful information about the process thanks to the strengths of the HVG method that manages to maintain the intrinsic characteristics by mapping each time series conserving its properties, as long as exponential behaviors are obtained and the fitting zone is properly chosen to determine the γ-degree. Independent of the limit, it is a useful technique for a systematic analysis of long- and short-range stochastic processes with the right criteria in the fitting domain (k range).

2.3. Kullback-Leibler Divergence D

Degree distributions P_{in} and P_{out} separately classify the succession between past and future events; that is, they provide information about the temporal irreversibility of the associated series. At the same time, they provide a relation with the entropy production of the physical mechanism generating the series [39]. A rigorous way to measure the difference between two degree distributions is through Kullback–Leibler divergence, which is a statistical measure of "distinguishability" [17] to quantify the degree of temporal irreversibility. The KLD between two probability functions is defined as [22]

$$D[P_{\text{out}}(k)||P_{\text{in}}(k)] = \sum_k P_{\text{out}}(k) \log \frac{P_{\text{out}}(k)}{P_{\text{in}}(k)}, \tag{2.5}$$

i.e., it is the weighted average of the logarithmic difference between the P_{out} and P_{in} probabilities, where the average is taken using the P_{out} probabilities. The divergence

is expressed with the natural unit of information when the logarithm is in base e. The KLD is always positive by definition (can be proved using Jensen's inequality [40]) and is vanishes if and only if $P_{\text{in}} = P_{\text{out}}$. As D moves away from zero, the distance between the distributions increases and with it the irreversibility of the series. Since it is not symmetrical, it is not a real distance measurement.

Each system under study provides different algorithmic challenges, depending essentially on the number of data provided by its time series. Obtaining this measure in some cases is not practical if we are strict to the definition when there are some cases in which $D \to \infty$ if $P_{\text{in}} = 0$. Thus, we propose and agree on the following conventions for each system discussed in this thesis.

For the case of PIC simulations in Chapter 3 and solar wind in Chapter 4: Since D is a weighted average between differences, the cases where, for some k, $P_{\text{out}}(k) > 0$ and $P_{\text{in}}(k) = 0$, we will consider it as a null contribution instead of infinity, since there is no probability to compare with, which in the result sometimes generates negative values in D. If this is the case, we define it as an outlier and discard it.

For the case of blazars in Chapter 5: We must take into consideration that some events are unseen, especially when dealing with observational data with short duration and gaps. While the presence of gaps is not a problem for the HVG, it is not prudent to assume every event as absolutely impossible. Therefore, we reassign a new, very low, probability when it is zero. The cases where $P_{\text{out}} = 0$ are contained in the definition itself. So, to cover the other cases, we smooth the probabilities **in** assigning a probability less than the minimum $P_{\text{in}}^{\min}$ in the form $P_{\text{in}}^{\min}/n$ when for certain k the probability is zero, and we subtract this new probability from the others to rescale. These considerations will allow us to compare degrees between spectral classes of blazars.

Chapter 3

Plasma Simulations

In a turbulent collisionless plasma (in which Coulomb collisions are neglected), movement on a kinetic scale (spatial scales of the order of the particles Larmor radius or skin-depth) occurs in a chaotic manner, and is determined by large-scale collective behavior and also localized small-scale processes. This kind of system can be commonly found throughout the Universe. The solar wind and the Earth's magnetosphere correspond to natural plasma physics laboratories in which plasma phenomena can be studied [41]. Some non-linear phenomena include magnetic reconnection [42], collisionless shocks [43], electromagnetic turbulence [44], collisionless wave-particle interactions [45], or plasma energization and heating [46]. One of the fundamental open questions in plasma physics is the understanding of the energy equipartition between plasma and electromagnetic turbulence, and the role of non-thermal plasma particles distributions ubiquitous in poorly collisional plasma environments.

One of the most used approaches to model non-thermal plasma systems is through the representation of the plasma velocity distribution function (VDF) using the well-known Tsallis or kappa distributions. First proposed by Olbert [47] and Vasyliunas [48] to fit electron measurements in the magnetosphere, it is accepted that kappa distributions are the most common state of electrons [see e.g. 49, 50],

and have been observed in space in the solar wind [51, 52], the Earth's magnetosphere [53, 54] or other planetary environments [55]. These distributions resolve both, the quasi-thermal core and the power-law high energy tails measured by the κ parameter, and correspond to a generalization of the Maxwell-Boltzmann distribution, achieved when $\kappa \to \infty$. Kappa distributions have been widely studied in the framework of non-equilibrium statistical mechanism as corresponding to a class of expected probability distribution function when the system exhibits non-extensive entropy [56–58]. Regarding plasma physics, it has been found that in kappa-distributed plasmas, the non-thermal shape of the distribution function plays a key role in the details of kinetic processes such as wave-particle interactions [59, 60], that mediate the collisionless relaxation of unstable plasma populations [61–63]. Moreover, even in the absence of instabilities, in a plasma with finite temperature, the random motion of the charged particles composing the plasma produces a finite level of electromagnetic fluctuations. These fluctuations, known as quasi-thermal noise, can be explained by a generalization of the Fluctuation-Dissipation Theorem [see e.g. 64, 65, and references therein], and have been studied in the case of thermal and non-thermal plasma systems. Recent results have shown that the fluctuations level in plasmas including supra-thermal particles following a kappa distribution is enhanced with respect to plasma systems in thermodynamic equilibrium [31, 65, 66].

Regardless of the nature of the distribution function (thermal or non-thermal), plasmas show a self-organized critical behavior [67] allowing the introduction of concepts from complex systems to studying this criticality. Those methods are applied both in data sets and models [68–71]. Some authors have suggested that the change of fractals and multifractals indexes could be associated with dissipative events or related to the solar cycle, proposing a relation between multifractality and physical

processes in plasmas related to the solar cycle, the Sun-Earth system or theoretical models of plasmas [68, 72]. Other studies show a relation between intermittency fluctuations and multifractal behavior, while the fluctuations at kinetic scales reveal a monofractal behavior [73–75]. Wawrzaszek et al. [72] apply a multifractal formalism to the solar wind suggesting a relation between the intermittency and the degree of multifractality. Those studies show different time series analyses in plasmas. But not only fractals and multifractals could be useful in the study of time series, complex networks, particularly the Visibility Graph method, allow a simple and direct time series analysis in self-organized critical phenomena, such as earthquakes [18], macroeconomic systems [9] or biological systems [10].

In the field of space plasma physics, the VG has been applied to solar flares [12, 13] and solar wind measurements [19]. In particular, Najafi et al. [13] show a complete and detailed analysis of solar flares through a combination of two methods of complex networks: a time-based complex network supported by the work of Abe and Suzuki [76] and the VG method proposed by Telesca and Lovallo [11]. They characterize solar flares based on the probability distribution of connectivity and clustering coefficient, finding a good agreement with results obtained in other works with seismic data sets. In addition, Suyal et al. [19] studied the irreversibility of velocity fluctuations. Through the HVG method, they calculated the KLD of the fluctuations and found that irreversibility in solar wind velocity fluctuations shows a similar behavior at different distances from the Sun, and that there is a dependence of the KLD with the solar cycle. Under this context, the results by Acosta et al. [77] have suggested that the use of the HVG method can provide valuable information to characterize turbulence in collisionless plasmas and that the KLD may be used as a proxy to establish how thermal or non-thermal are the velocity distributions of a plasma,

only by looking at the magnetic fluctuations and their properties.

Here we build a complex network based on the HVG technique [17] applied to magnetic field fluctuations time series obtained from Particle In Cell (PIC) simulations of magnetized collisionless plasma. We analyze the degree of irreversibility of magnetic fluctuations self-generated by the plasma, comparing the case of a thermal plasma (described by a Maxwell-Botzmann VDF) with the fluctuations generated by non-thermal kappa distributions. In order to understand the degree of irreversibility as a parameter that could be related to the shape of the particles' velocity distributions, we computed the KLD for different values of the κ parameter for comparative purposes and analyzed their time evolution throughout each simulation. The chapter is organized as follows. Section 3.1 shows the model used to build the time series, and in Section 3.2 the results are presented.

3.1. Thermal and non-thermal plasma particle distributions

To build time series of magnetic fluctuations produced by a collisionless plasma we performed PIC simulations. The simulations treat positive ions and electrons as individual particles that are self-consistently accelerated by the electric and magnetic field through the charge and current densities collectively produced by themselves. For our study, we consider a so-called 1.5D PIC code, that resolves the movement of the particles in one dimension but computes the three components of the velocity of each particle, and therefore the three components of the current density. Our code has been tested and validated in several studies [see e.g. 78, 79], and technical details about the used numerical schemes can be found in [31].

We simulate a magnetized plasma composed by electrons and protons with mas-

ses m_e and M_p, respectively, and realistic mass ratio $M_p/m_e \sim 1836$. We assume the warm plasma as quasineutral, in which both species have number density n_0, such that $\omega_{pe}/\Omega_e = 5$. Also, $\omega_{pe} = (4\pi n_o e^2/m_e)^{1/2}$ is the plasma frequency, $\Omega_e = (eB_0)/(m_e c)$ is the electron gyro-frequency, e is the elementary charge, c the speed of light, and B_0 is the background magnetic field. Our code solves the equations in a one-dimensional grid with periodic boundary conditions, and the background magnetic field aligned with the spatial grid ($\mathbf{B_0} = B_0\hat{x}$). To resolve the kinetic physics of electrons we set up a grid of length $L = 256\,\lambda_e$, where $\lambda_e = \omega_{pe}/c$ is the electron inertial length. We divide the grid into $N = 2048$ cells, initially with 1000 particles per species per cell, and run the simulation up to $t = 1330.72/\Omega_e$ in time steps of length $dt = 0.01\Omega_e$. For each simulation, we initialize the velocities of the particles following an isotropic VDF $f_j(v)$, with $j = e$ for electrons and $j = p$ for protons, and v represents the velocity. For the case of a plasma in thermodynamic equilibrium, f_j corresponds to a Maxwell-Boltzmann distribution

$$f_j(v) = \frac{n_0}{\pi^{3/2}\alpha_j^3}\,\exp\left(-\frac{v^2}{\alpha_j^2}\right)\,, \tag{3.1}$$

and in the case of a non-thermal plasma f_j is given by a kappa distribution. Namely:

$$f_j(v) = \frac{n_0}{\pi^{3/2}\alpha_j^3}\,\frac{\Gamma(\kappa_j)}{\kappa_j\Gamma(\kappa_j - 1/2)}\left(1 + \frac{1}{\kappa_j}\,\frac{v^2}{\alpha_j^2}\right)^{-(\kappa_j+1)}\,. \tag{3.2}$$

Here, $\alpha_j = (2k_B T_j/m_j)^{1/2}$ is the thermal velocity of the distribution, κ_j and T_j are the kappa parameter and the temperature of each species, and k_B is the Boltzmann constant. Also, Γ corresponds to the Gamma function, and note that kappa distributions (Equation (3.2)) becomes the Maxwell-Boltzmann distribution (Equation (3.1)) in the limit $\kappa \to \infty$. However, for kappa values $\kappa \gtrapprox 10$ the kappa and Maxwellian VDFs are relatively similar.

Following all these considerations, for our study we run and compare the results of three different simulations with different values of the electron κ_e parameter. Case 1: a plasma in thermal equilibrium with electrons following a Maxwell-Boltzmann distribution given by Equation (3.1); case 2: non-thermal electrons following Equation (3.2) with $\kappa_e = 3$, representing a system far from thermodynamic equilibrium; and case 3: a plasma with $\kappa_e = 15$, also non-thermal but closer to equilibrium. In addition, to isolate the effects of thermal or non-thermal electrons, for all three cases we consider protons following a Maxwellian; i.e. $\kappa_p \to \infty$. Finally, for all cases, we consider a plasma with temperature T_j, such that the plasma beta parameter is $\beta_j = 8\pi n_0 k_B T_j / B_0^2 = 0.01$ for both species; i.e. $\beta_e = \beta_p = 0.01$.

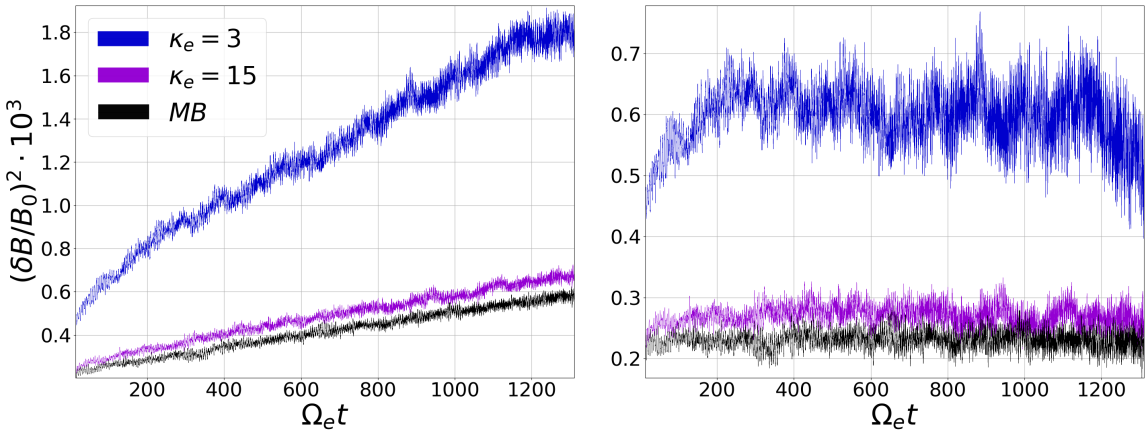

Figure 3.1: (Left) Average magnetic field energy density fluctuations $(\delta B/B_0)^2$ as a function of time obtained from PIC simulations for Maxwell-Boltzmann (where MB represents $\kappa_e \to \infty$) and kappa distributions considering different values of the κ_e parameter. (Right) Detrended average magnetic field energy density magnitude.

As already mentioned, even though a collisionless isotropic plasma is a system at equilibrium according to the Vlasov Equation, the plasma will develop a certain level of magnetic fluctuations spontaneously produced by the motion of the charged particles [31, 64–66]. This is precisely the situation of our study for any of the three

simulations (three cases) we have performed. Figure 3.1 shows the average magnetic field energy density fluctuations $(\delta B/B_0)^2$ as a function of time, for all three cases. To build these time series, at each time step we have computed the transverse magnetic fluctuations at the plane perpendicular to $\mathbf{B_0}$ and have averaged the magnitude of the fluctuations at each grid point. Figure 3.1 (left) shows the fluctuation time series for $\kappa_e = 3$ (blue), $\kappa_e = 15$ (purple), and the $\kappa_e \to \infty$ or Maxwell-Boltzmann distribution (black). As expected, we can see that the level of fluctuations increases with decreasing value of κ_e and that the behavior of the fluctuations with $\kappa_e = 15$ is fairly similar to the Maxwellian case. In addition, Figure 3.1 (right) presents the time series of the detrended fluctuations, where we can see that the amplitude of the fluctuations also increases as κ_e decreases. In the next section, the HVG method will be applied to all these time series.

3.2. Results

We apply the HVG method to study the time series of magnetic fluctuations obtained from the PIC simulations. Considering the Maxwellian and kappa distributions, we follow the HVG algorithm and build complex networks for three cases: Maxwellian distribution (thermal equilibrium with electrons), $\kappa_e = 3$ (non-thermal electrons), $\kappa_e = 15$ (non-thermal electrons, but closer to the equilibrium), using the original and the detrended time series (see Figure 3.1). We calculate the in-going and out-going degrees for the time series to characterize their distribution for each case.

First, if we now focus on the UHVG, where $k(i) = k_{\text{in}}(i) + k_{\text{out}}(i)$, we obtain the undirected degree distribution $P(k)$ (Section 2.2). Figure 3.2 shows an exponential distribution for the degree distribution for the three cases studied, this is understood as do to short-range exponentially decaying correlations, where γ corresponds to the

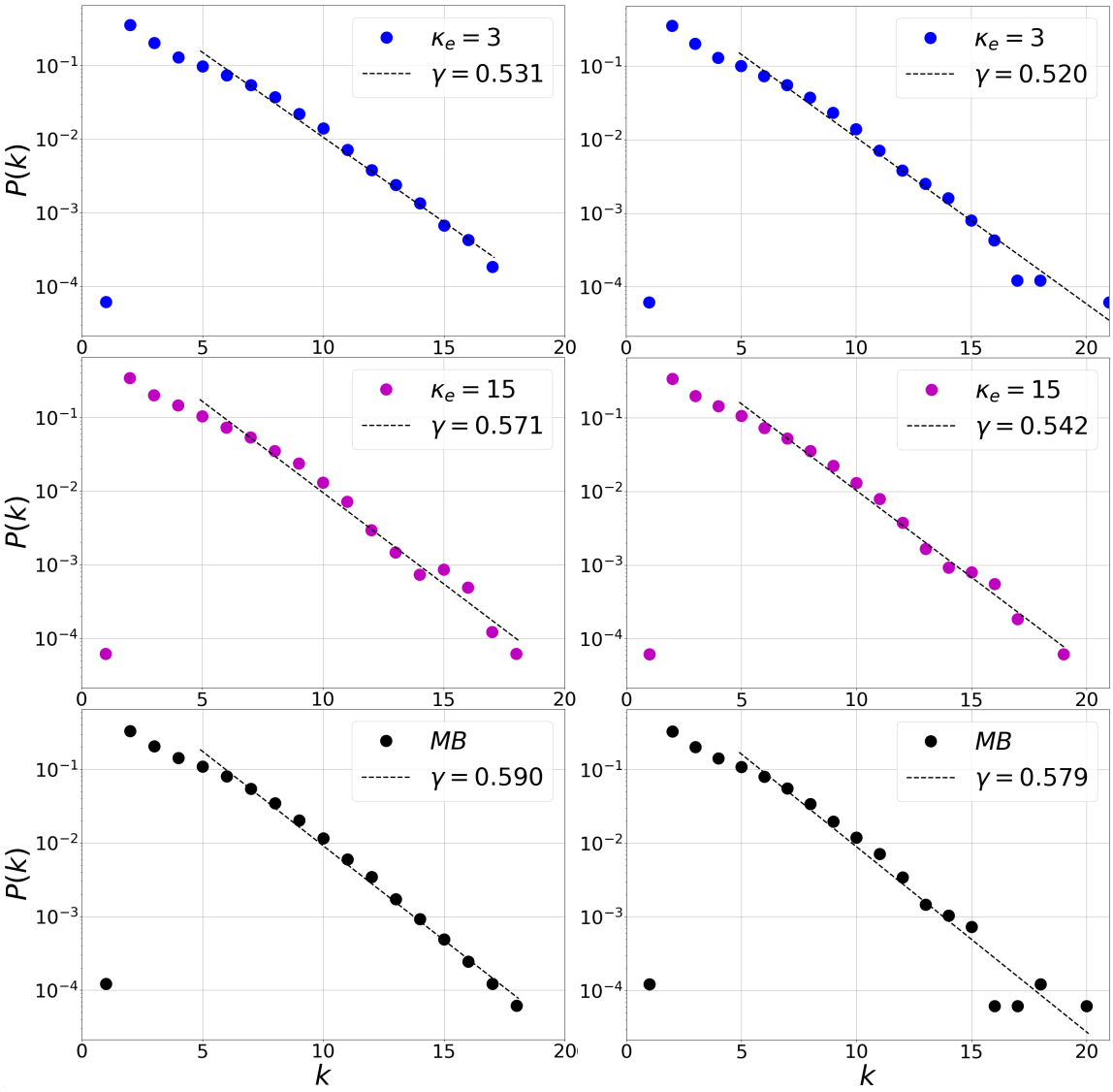

Figure 3.2: Semi-log plot of the degree distributions of HVG associated with kappa and Maxwell-Boltzmann distribution. There is an exponential behavior $P(k) \sim \exp(-\gamma k)$ and the γ value is shown for each distribution. The left panel corresponds to the results for the magnetic field of the trend data from Figure 3.1 (left), while the right panel corresponds to the detrended data from Figure 3.1 (right).

slope of the linear fit in the semilog plot of the degree distribution (Equation 2.4). The values of the slope are computed considering the tail of the distribution [11] in Figures 3.2, in this case from the degree $k = 5$ up to the largest value of k at each

plot. The values of the slope are between $\gamma = 0.531$ ($\kappa_e = 3$) and $\gamma = 0.590$ (Maxwell-Boltzmann distribution), in the case of trended data and between $\gamma = 0.520$ ($\kappa_e = 3$) and $\gamma = 0.579$ (Maxwell-Boltzmann distribution), in the case of detrended data sets. We observe that for each value of the slope, it is satisfied that $\gamma > \gamma_{\text{un}}$. This suggests us all series correspond to correlated stochastic processes from which we can extract consistent information. Also, the trend does not seem to greatly affect these correlations.

Second, considering the DHVG we have computed the Kullback-Leibler Divergence, D from Equation 2.5, for each case mentioned before. The values of the divergence D are in Figure 3.3 compared to standard deviation σ (vertical bars in the figure) calculated from the algorithm applied on the randomly disarrayed data [see e.g. 18, and references therein]. In this algorithm, the original data is randomly shuffled to obtain a large number of disordered copies (in this case 1000 copies) of the original data set, and the divergence D is computed for each copy. The vertical lines in Figure 3.3 correspond to the average value of the divergence D of all copies (central value) plus and minus a standard deviation. After this procedure, if the D value is contained inside the σ bar, the time series represents a reversible process. This is because by randomly disarraying the series and obtaining the same results regardless of the temporal order of the data set, it is indicating that the information corresponds to a reversible process. On the contrary, if D is outside the vertical range defined by the random copies, then the value of D is statistically significant, and therefore it is possible to state that the data set indeed represents an irreversible process.

Figure 3.3 shows that the dissipative degree of the system increases as the value of κ_e decreases and the distribution function departs from the Maxwell-Boltzmann equilibrium. In Figure 3.3 (left), the processes for $\kappa_e = 15$ is reversible, case close

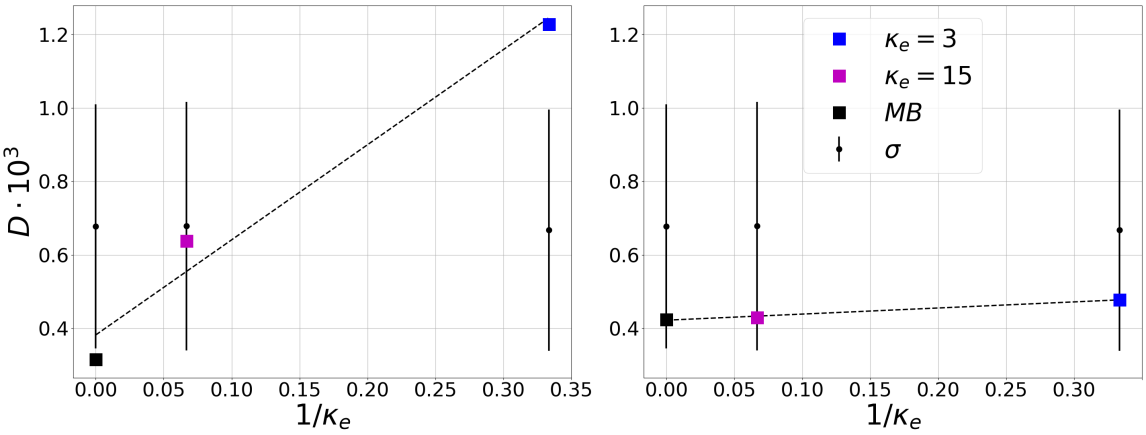

Figure 3.3: KL-Divergence (D) for the magnetic field time series with different kappa distributions. (Left) HVG method applied on the original data. (Right) HVG on the detrended data. The technique used to determine whether the data represent a reversible process consists of applying the HVG algorithm to randomly disordered copies of the data, obtaining the standard deviation σ around the average divergence computed using the disordered data (black dot and vertical lines).

to thermal equilibrium. Meanwhile, in Figure 3.3 (right) all distributions correspond to reversible processes by reducing the background trend. This last result could be explained due to the fact that, independent of the value of κ_e, all considered distributions are steady state solutions of the Vlasov equation. Finally, to further analyze the relationship between the κ parameter and the KLD, we compute the time evolution of D as shown in Figure 3.4. Figure 3.4 (right) shows the same behavior found above, exhibiting a decrease in the value of the divergence for the Maxwellian distribution, whereas for $\kappa_e = 3$ this value tends to increase. That is, given the initial conditions of the simulation, $\kappa_e = 15$ and Maxwellian coincide in their behavior over time towards a low degree of divergence, while $\kappa_e = 3$ presents a behavior to the opposite extreme.

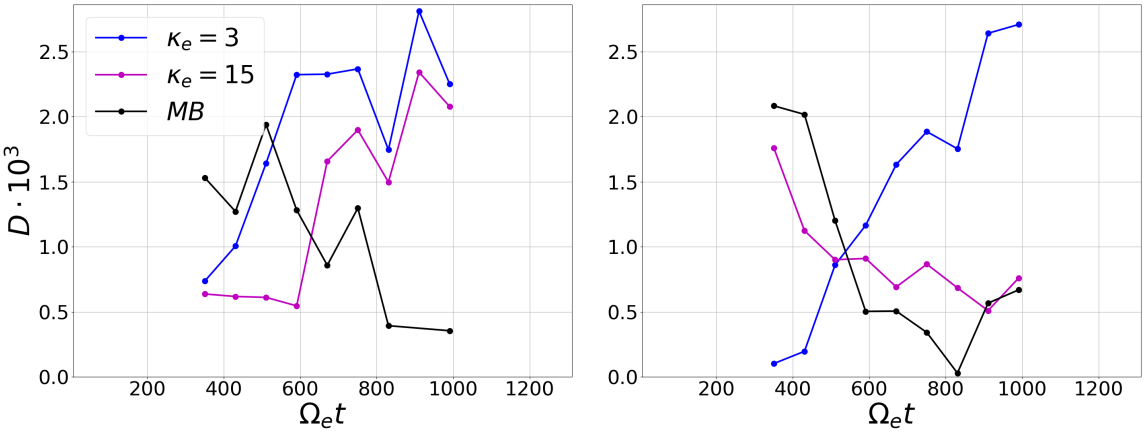

Figure 3.4: Temporal evolution of the KL-divergence considering a moving window that covers 8000 data overlapping every 1000 data on the magnetic time series. (Left) HVG method was applied on the original data and (right) on the detrended data.

Chapter 4

Solar Wind

Several different dynamics exist when studying solar wind depending on its origin and the distance to the Sun. To discriminate and classify solar wind type between slow and fast, we can consider five relevant parameters, such as radial velocity, proton density, proton temperature, the oxygen ion ratio, and the magnetic compressibility factor [80]. All these relevant parameters reflect the dynamic of the solar wind while this is in expansion from the continuation of the solar corona until being in contact and interacting with the Earth's magnetosphere. In this path, this plasma reaches velocities among $250-800\,\mathrm{km\,s^{-1}}$ approximately, and at the same time, this is subject to the solar activity cycle of approximately 11 years and the solar magnetic cycle of approximately 22 years (the Hale cycle) [81]. During its expansion, the solar wind develops a strong turbulent character [82]. Wherever the solar wind is observed, there are many non-linear phenomena involved in many scales.

The turbulence property is assigned to indicate that something behaves outside what can be understood as regular. *"The behavior of a flow that rebels against the deterministic rules of classical dynamics is called turbulent"* [82]. Turbulence in the solar wind has been subject to study for different models of systems science. Wawrzaszek et al. [80] have developed a multifractal study of the intermittency of the

magnetic field turbulence in the solar wind measured by Ulysses spacecraft, based on a comprehensive data selection criteria to discriminate between the state of the slow and fast solar wind not only with the velocity parameter. They reported a slow decrease of intermittency with radial distance, and that the slow solar wind at solar cycle 23 maximum exhibits a lower level of multifractality than the fast solar wind. They justify the radial dependence of the multifractality by a slower evolution of the turbulence beyond the ecliptic plane and by the lower efficiency of the intermittency drivers with distance from the Sun. As for the distinction of the wind type with respect to the cycle, they relate it to the idea of a new type of slow Alfvénic solar wind.

The occurrence of intermittency in plasma turbulence has been well explored by studying the deviation from the Gaussian distribution of the PDF for both velocity and magnetic fluctuations [83–85]. Other studies show a relationship between intermittency fluctuations and multifractal behavior as the result of the multifractal properties of the solar wind turbulent cascade [86], while kinetic-scale fluctuations reveal monofractal behavior [73, 75, 87], as opposed to multifractality.

The Lyapunov exponent has been widely used in the analysis of the dynamics of space plasmas. Gupta et al. [28] and Redaelli and Macek [27] have studied the Lyapunov exponent of velocity fluctuations measured by the Helios spacecraft. Gupta et al. [28] analyzed the time series of the solar wind speed fluctuations to understand the local dynamics of the slow wind speed fluctuations. They analyzed the Lyapunov exponents and suggested that there are inherent changes in the dynamics throughout solar cycle 21, and that there is low-dimensional chaotic behavior in the underlying dynamics. Redaelli and Macek [27], Macek and Redaelli [88] analyzed the fluctuations of the low-speed stream of the solar wind using a nonlinear filter to approximate

the nonlinear behavior of the flow, and also obtained more reliable estimates of the Lyapunov exponent and the Kolmogorov entropy. Through their results, they found that the solar wind in the inner heliosphere is probably a deterministic chaotic system.

Continuing with natural complexity measures to detect dynamic changes in time series, Suyal et al. [26] calculated the permutation entropy of the solar wind time series at different phases of solar activity cycle 23. They worked with measurements obtained by the ACE spacecraft and observed that the complexity of the solar wind velocity fluctuations at 1 AU is dominated by the hysteresis phenomenon when following the ascending and descending phases of the solar cycle. This induced them to suggest the presence of multistability in the dynamics governing the solar wind speed throughout a solar activity cycle. Then, Suyal et al. [19] estimated the Kullback–Leibler Divergence of the solar wind velocity via complex networks. They analyzed solar wind speed measurements obtained by the ACE and Helios spacecraft and calculated the KLD at different phases of the solar activity cycles 21 and 23. Their work concluded that the solar wind speed is more variable during the maximum and minimum activity phases, while it is less variable during the ascending and descending phases of the solar activity cycle, and the irreversibility parameter (KLD) over a solar activity cycle is similar to 0.3 AU and 1 AU.

These studies support the non-universal and complex nature of solar wind turbulence. Complex networks are a tool that often describes the origin of complexity in complex systems. Systems science analysis can work even before much of the physics can be assimilated and integrated [89].

This chapter is organized as follows. Section 4.1 explains a summary of the significant features of observations and characteristics of solar phases along solar cycles

23 (SC23) and 24 (SC24). Then, Section 4.2 exposes our results after applying the HVG method on magnetic time series.

4.1. Solar wind and solar cycles

The solar wind is a stream of charged ions and electrons that escape from the solar corona rapidly and continuously into the interplanetary medium. It is a combination of a slow, dense, and highly variable at lower heliolatitudes, and also a faster, tenuous, and uniform wind at high heliotitudes [90–93]. 75 % of the solar wind velocities show a value on the order of $530.38 \pm 2.22\,\mathrm{km\,s^{-1}}$ for SC23 [94]. If we focus on solar wind classification based on speed, the slow solar wind would be in the range 300–$450\,\mathrm{km\,s^{-1}}$, and the fast wind between 500–$800\,\mathrm{km\,s^{-1}}$. The fastest streams, i.e., fast solar wind, can travel from the Sun up to 1 AU in $\approx$ 2.0–3.5 days [95]. The slow solar wind originates above the active regions on the Sun and tends to be highly structured. While the fast wind, plasma originating from polar coronal holes, is usually considered to be structure-free or relatively homogeneous [96]; however, according to more recent studies, it is not homogeneous [97]. What we certainly know is that the typical equatorial slow wind is more variable than the pure coronal fast wind.

The intercorrelation between solar activity and solar wind is a topic of fundamental importance. The global structure of the three-dimensional solar wind at solar maximum is completely different than at solar minimum [92]. The sunspot number is a synthetic index that quantifies the relationship between solar variability and its magnetic activity [98]. Thus, the sunspot number S_n is a direct indicator of solar activity, because its cyclic variations have been characterized by smoothed sunspot numbers as a first proxy for solar phases [99]. The Sun's magnetic activity increases

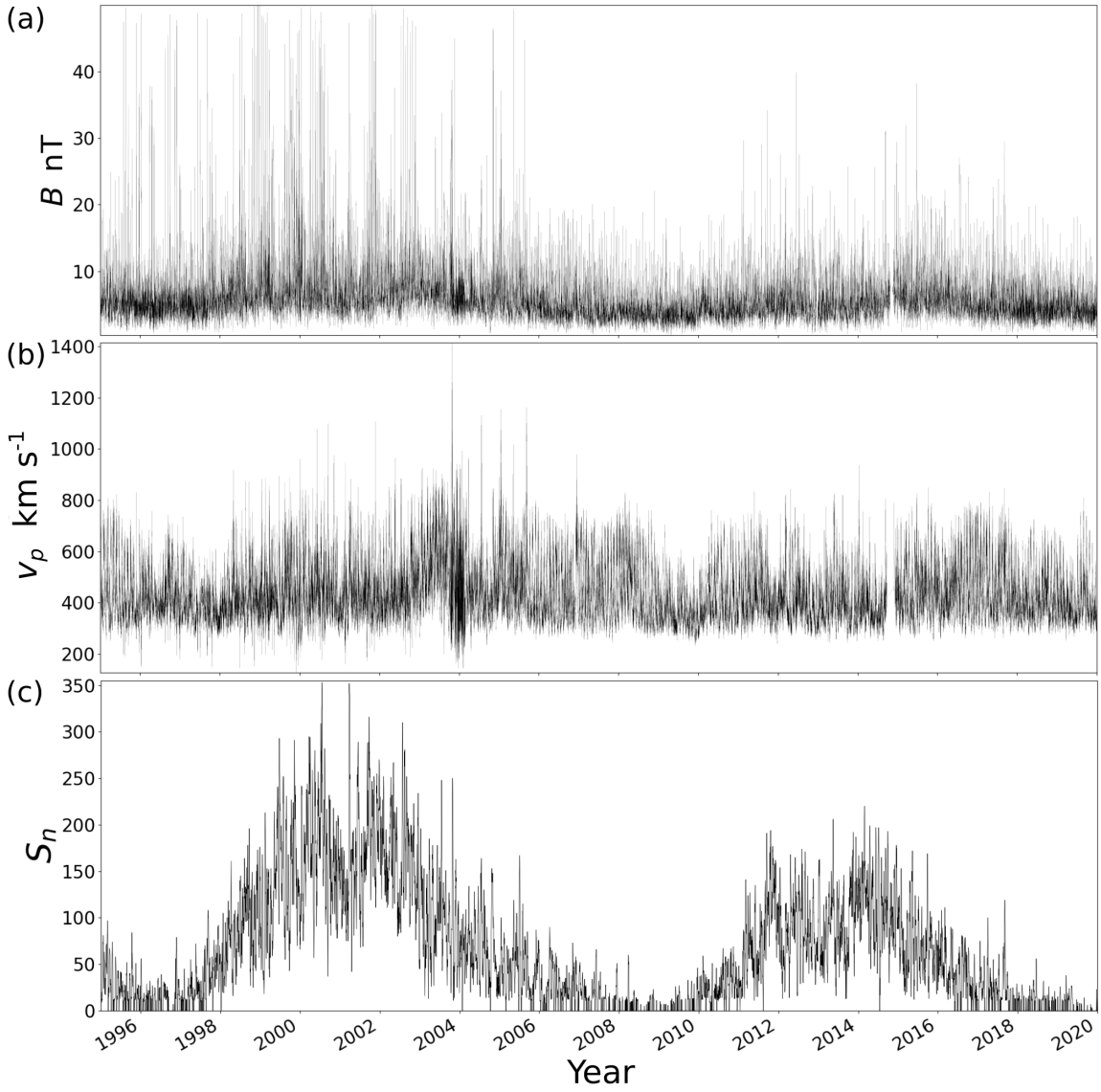

Figure 4.1: Time series of the data used in this study. This data set is composed of solar wind magnetic field (B in the top panel), as input for the HVG method, solar wind proton bulk speed (v_p in the middle panel), and sunspot number (S_n in the bottom panel), as variables for comparison. The first two data sets were obtained from NASA CDAweb by Wind Mission (observations at 1 AU), while the last data set was obtained from World Data Center SILSO by Royal Observatory of Belgium. The data shown correspond to measurements taken during the period from 1995-01-01 to 2019-12-31, covering solar cycles 23 and 24. B, v_p, S_n time resolution are 1 hour, 92 seconds and 1 day, respectively.

as solar activity does, which can be visualized in four phases: minimum, ascending, maximum, and descending [100, 101]. In particular, the solar minimum is a period of low magnetic activity in the Sun that occurs between the descending phase of the old cycle and the ascending phase of the new cycle. This transition is marked by the reversal of the magnetic activity gradient, a phase in which the Sun's magnetic field is completely flipped.

Compared to SC23, SC24 exhibited the lowest activity. The previous five cycles had been notably productive in terms of sunspots, but SC24 was not. The minimum phase transition between SC23 and SC24 took a longer period than usual (2007-01-07 to 2009-10-31), and reached the lowest level in about a century, specifically since 1913. This can be understood due to the slow decrease in the activity of SC23 and the slow increase in SC24. This decrease in Sun's activity was also manifested in the solar magnetic field variations [102], as the interplanetary magnetic field showed very low values during the years of the minimum. The observations made in the near-Earth ecliptic plane were also surprisingly the lowest values in the *in situ* solar wind measurements from 1963 until then, according to the OMNI database compilation. Therefore, this very particular cycle change offers a special opportunity to base our study on the comparative search for intercorrelations with complexity parameters.

We work with magnetic field and proton bulk speed data measured by the Magnetic Field Investigation (MFI) [103] and the Solar Wind Experiment (SWE) [104] instruments onboard the Wind spacecraft, which provides observations of the ecliptic plane (obtained from NASA CDAweb); and with sunspot number obtained from World Data Center SILSO. We use one-hour cadence Wind-MFI data to characterize magnetic field measurements at 1 AU. The data set corresponds to measurements taken during the period from 1995-01-01 to 2019-12-31, so it includes the end of

SC22, completely covers cycles 23 and 24, and the beginning of SC25. We focus on SC23 and SC24. SC23 dates from 1996-05-06 to 2008-11-23, and SC24 dates from 2008-11-24 to 2019-11-24, according to the cycle and phase start and end dates specified by Reyes et al. [101]. Figure 4.1 displays the time series of the data set used in this study, where Figure 4.1a shows the solar wind magnetic field used as input for the HVG method, Figure 4.1b shows the proton bulk speed with a 92-second cadence, and Figure 4.1b shows the daily sunspot number. In our analysis, the latter two are used as variables for comparing the behavior of solar wind and solar activity.

4.2. Results

This study modeled the time series of magnetic fluctuations data collected from the Wind satellite observations as HVGs over time. For this purpose, moving windows in time were used, covering approximately two months of magnetic data (1440 data/nodes covered by each network), with an overlap of approximately one day (the distance between data windows is 24 data/nodes). The moving windows begin in 1995-01-01, and when the series cannot contain the same amount of 2-month data towards the end of the series, the calculation is stopped. Each of these windows encapsulates the data information. In that way, we map it into a network under the geometrical criterion of horizontal visibility. Thus through this mapping, we built every complex network with the same amount of nodes and assign it the mean of the time interval covered by the moving window. Every network has a degree distribution P given by the undirected HVG and two degree distributions, P_{in} and P_{out}, from directed HVG. From these, we calculated the γ (Equation 2.4) and D (Equation 2.5) values in time using data shown by Figure 4.1a. As mentioned in Section 2.3, there are a few points where D can be negative. For the data analyzed, this occurs in only

4 % of the networks (39 out of 8959 moving windows), so we discard these cases, which is consistent with them being considered outliers, as defined in Section 2.3. Figure 4.2 contains the temporal evolution of these parameters for the magnetic field. In Figure 4.2a, the limit $\gamma_{\text{un}} \approx 0.405$ between correlated stochastic and chaotic time series [16] is indicated (as defined in Section 2.2), and the error in γ, σ_γ, was calculated from the exponential fit. In addition, for each window, networks have been constructed from 1000 randomly disordered copies of the data. Thus, Figure 4.2b plots the standard deviation σ_{rev} and average D for each window, in order to have an estimate of the level of reversibility. γ is almost always above the limit, and D goes in and out of the reversibility range.

The information in Figure 4.3 allows us to infer a statistical analysis of our results relative to the behavior of the solar wind through the solar cycles. In Figures 4.3a–b regarding information for unclassified solar wind, i.e., solar winds combined. On average and in terms of cycles, the γ exponent was higher for SC24, and the D divergence was higher for SC23. Also, D measure appears to vary as a function of phase. However, the γ value does not vary much, as all values within the central quartiles are concentrated around $\gamma = 0.5 > \gamma_{\text{un}}$. These latter results suggest that these are predominantly correlated stochastic and not uncorrelated chaotic time series. When γ has a slight decrease, D increases and is prominent in the maximum phases, becoming lower in the minimum phases, and in the ascending and descending transitions, the values are intermediate. This encourages us to look deeper for correlations with solar activity.

We can also analyze in Figures 4.3a–b statistical information distinguishing fast wind from slow wind around the $500\,\text{km}\,\text{s}^{-1}$ threshold. The differences in both complexity measures between solar wind types are very small, but they exist and are at

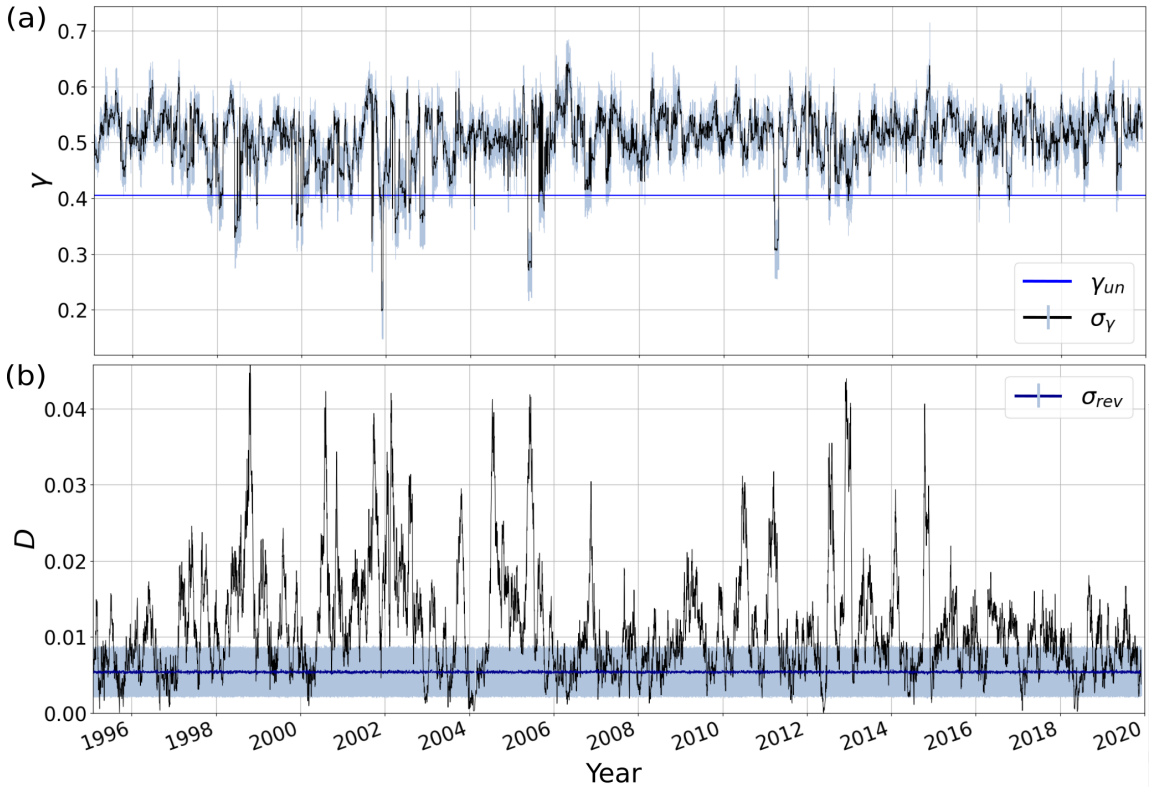

Figure 4.2: The black curve is the temporal evolution of (a) γ and (b) D of the magnetic field, considering a moving window that covers two months with a one-day overlap. (a) In the first case, the light blue color indicates the γ error, σ_γ, obtained from the linear fit of $\log(P(k))$. (b) In the second case, the light blue color indicates the reversibility range, that is, when we apply the HVG algorithm to randomly disordered copies of the data in every window, obtaining the standard deviation σ_{rev} around the average divergence (in dark blue) computed using the disordered data. The period is from 1995-01-31 to 2019-12-02, so covers SC23 and SC24.

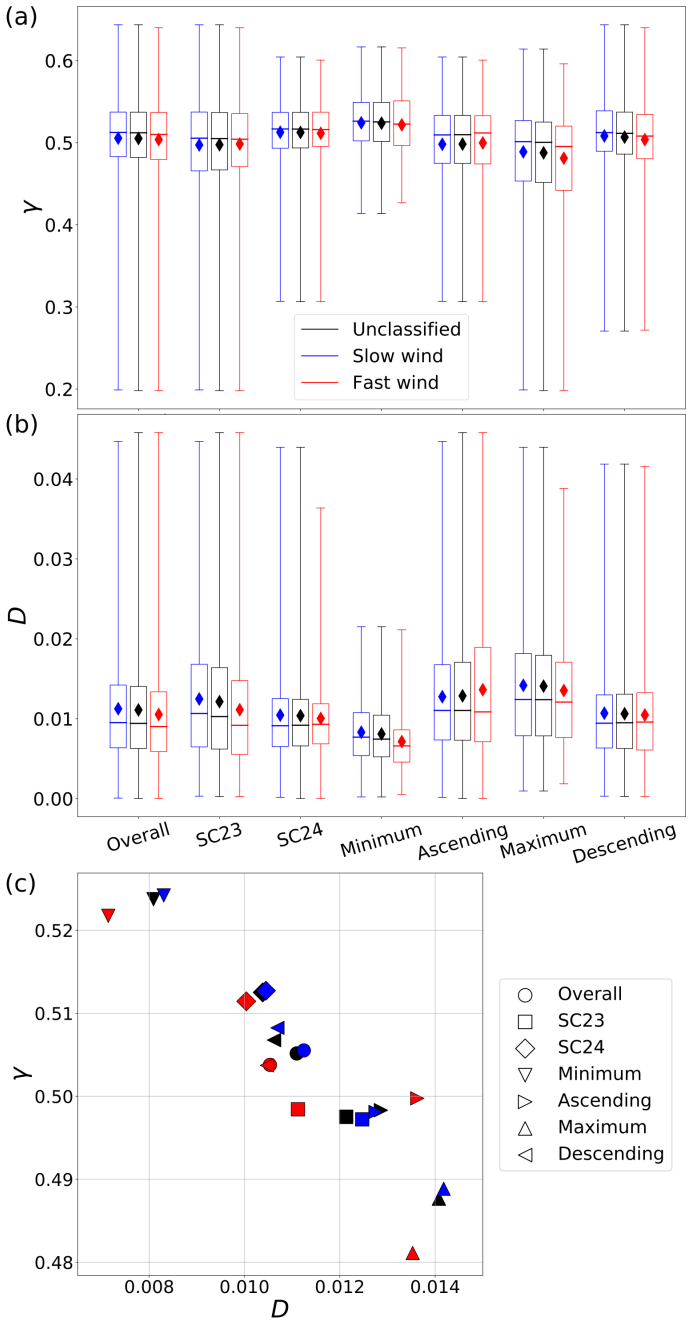

Figure 4.3: Solar wind: Boxplot diagrams in the first two panels show the mean (diamond symbol), median (horizontal line), and 25–75 % percentiles of (a) γ and (b) D values for overall data, by cycle, and by total cycle-independent phases, according to the following classification: slow/fast for solar wind speeds under/over 500 km s^{-1}. The whisker indicates the range between minimum and maximum values calculated. (c) Scatter plot of the means of γ and D values. Means for solar wind without classifying (black color), slow (blue color), and fast (red color) wind.

least more evident in the D divergence means than for the γ exponent means. Even with the classification between solar wind types, γ behaves similarly. On the other hand, D for both wind types, slow and fast, shows the same dependence on the solar phases, as for the unclassified wind (black boxplots). We can also realize that D is always slightly higher for slow wind than for fast wind, except in ascending phases. In general, the slow wind is highly variable, and the D divergence is characterizing it as the solar wind with the highest degree of irreversibility. If we plot just the mean values of Figures 4.3a–b (diamond symbols), Figure 4.3c verifies the anti-correlation between γ and D. The correlation coefficients between the complex parameters for the phase values only (i.e. if we focus on the triangles in Figure 4.3c are -0.992 for unclassified solar wind (black triangles), -0.998 for slow wind (blue triangles), and -0.882 for fast wind (red triangles). So, although the variations in γ are small, the anti-correlation between the two measurements is clear, as can be seen in Figure 4.3c. In addition, as can be seen in the same plot, the correlation between γ and D also depends on solar wind speed, and the highest anti-correlation corresponds to slow solar wind magnetic fluctuations (blue symbols in Figure 4.3c). More details about the values associated with the boxplots of Figure 4.3 are given in Tables 4.1 and 4.2.

We have also performed the analysis according to solar cycle phases. Figure 4.4 and 4.5 show γ and D in black curves, comparing them with S_n and v_p (in blue), respectively. In both figures, all curves have been smoothed by a yearly running average. The colored areas indicate the phases of the solar cycles and help us to distinguish the curves' behavior according to solar activity.

First, relative to the sunspot number, from Figure 4.4a we can see that γ exhibits anti-correlation with it especially within SC23. In general, the yearly smoothed curve

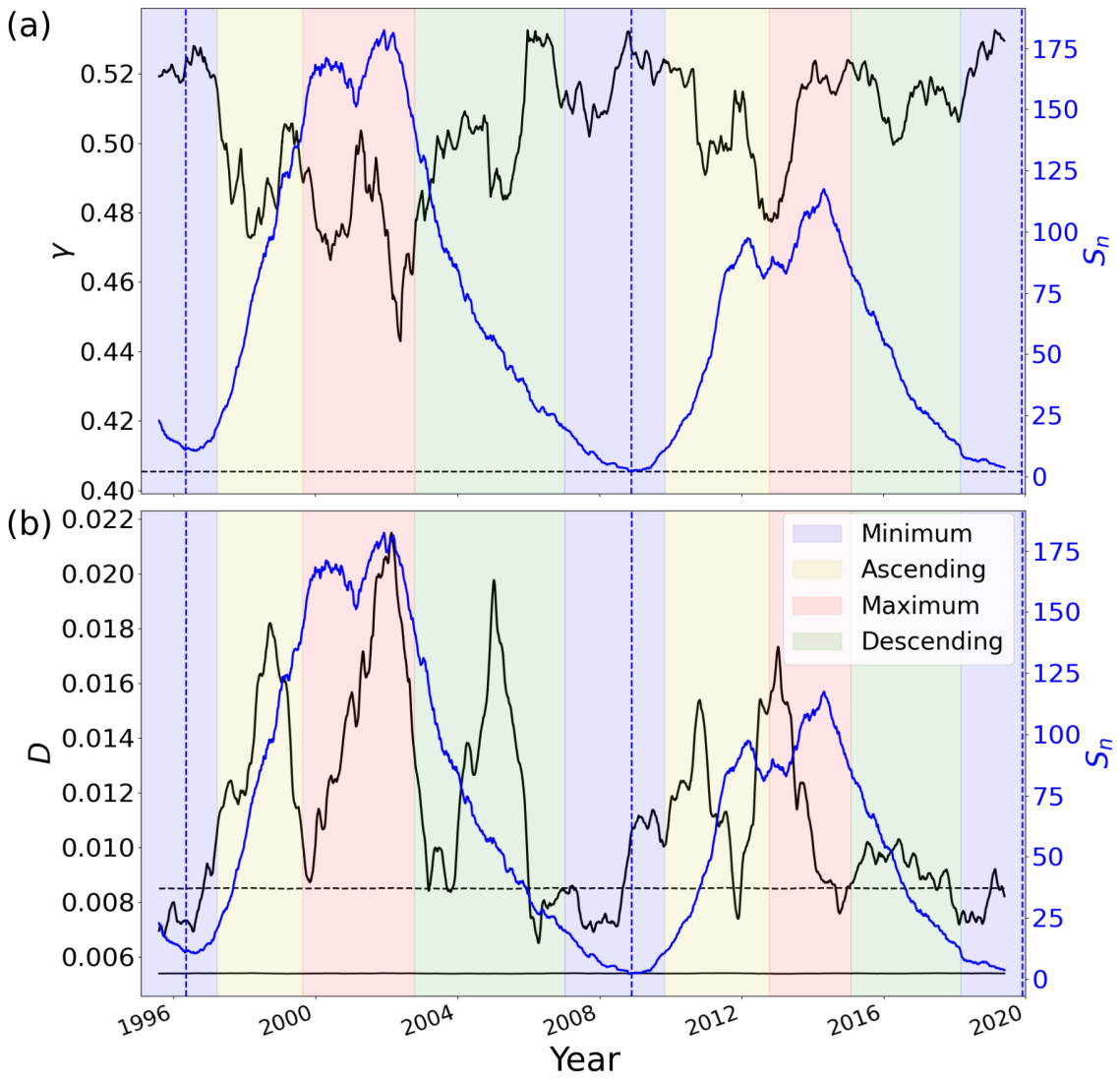

Figure 4.4: Solar activity: All curves are smoothed by a yearly running average of the values of γ and D (black curves) at the left, and S_n (blue curves) at the right. Horizontal dashed black lines indicate the limit $\gamma_{\mathbf{un}}$ between chaotic and stochastic information in (a), and indicate the upper half of the reversibility range over the continuous black line in (b). Vertical dashed blue lines delimit solar cycles 23 and 24. The colored blocks represent the phases of the solar cycles. The period now is from 1995-08-05 to 2019-05-29.

presents values above γ_{un}, suggesting that magnetic fluctuations time series correspond to correlated stochastic processes, observing also that the curve tends to decrease stochasticity as it approaches the maximum (it approaches the γ_{un} limit). From Figure 4.4b, we observe a particular match between the most prominent peaks of both curves in the maximum of SC23. In the maximum of SC24, the peak for the curve of D is in the gap between the double peaks of S_n. Also, the baselines (inferior envelopes) follow each other except for some delays, as in the ascending phase in SC24. At the minimum phases, the KLD values indicate reversible processes because the smoothed values of D are contained in the reversible range. Our results suggest a correlation between KLD and solar activity.

Second, relative to the proton bulk speed, in Figure 4.5a at the beginning of the SC23, during the minimum and ascending phases, γ and v_p are correlated, but in the following transitions, this behavior tends to be reversed, as opposed to D in Figure 4.5b, since it shows an anti-correlation with v_p from the beginning of the series, with few partial exceptions (the second half of the ascending phase in SC23, and the descending phase in SC24 for instance). In most of the phases both γ and D exhibit a certain anti-correlation with v_p in different manners.

The presence of clear correlations indicates the possible responsibility of a physical process relating to the quantities under study. To explicitly follow correlations through these physical measures and the parameters of the complex network extracted from magnetic time series of the solar wind, we tabulate correlation coefficients with their statistical significance overall (from 1995-08-05 to 2019-05-29), by cycle, and by phase in each cycle, in Tables 4.3 and 4.4. These tables precise what we have previously described from Figures 4.4 and 4.5, with more robust statistical results.

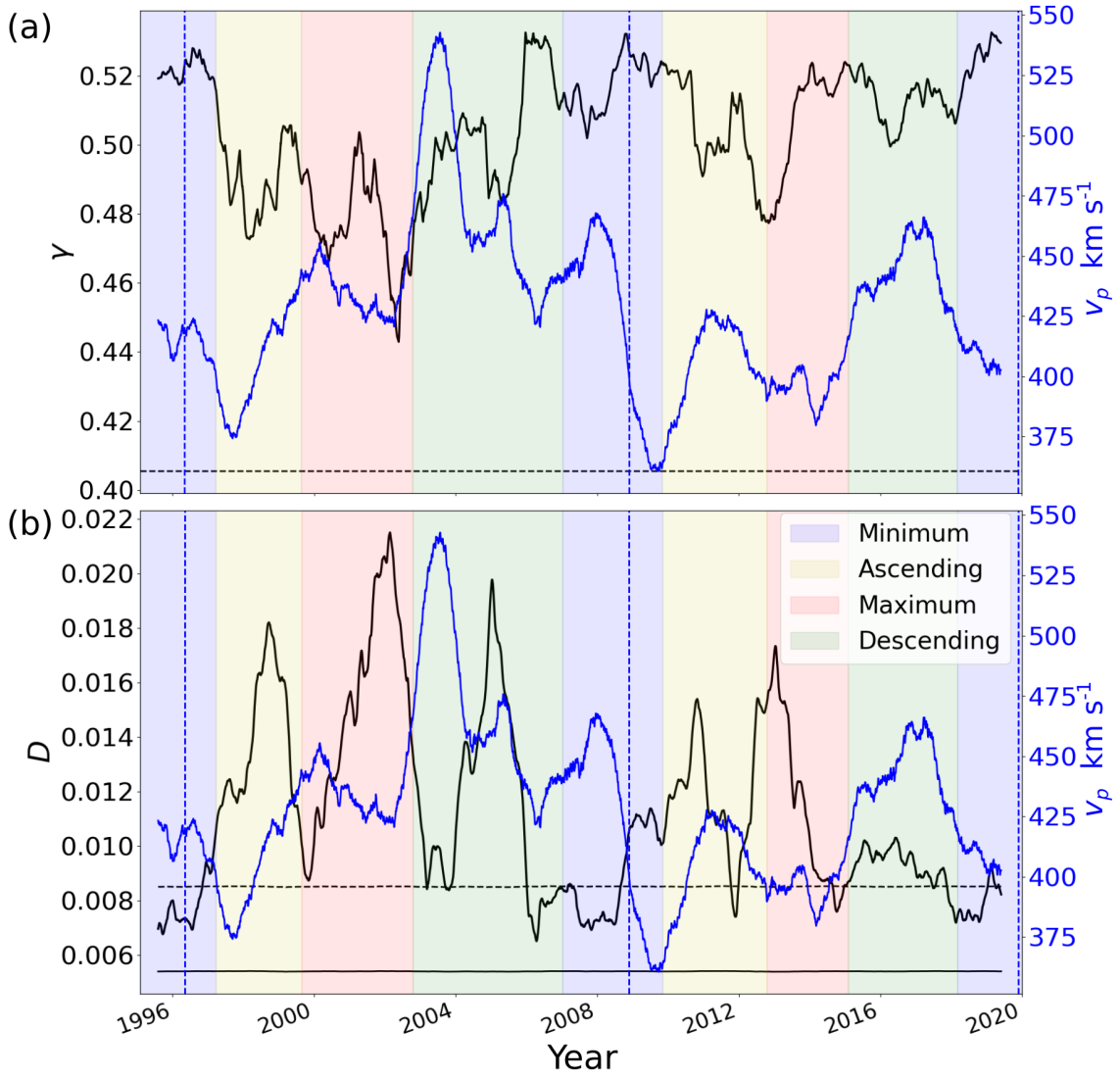

Figure 4.5: Solar wind speed: All curves are smoothed by a yearly running average of the values of γ and D (black curves) at the left, and v_p (blue curves) at the right. Horizontal dashed black lines indicate the limit $\gamma_{\mathbf{un}}$ between chaotic and stochastic information in (a), and indicate the upper half of the reversibility range over the continuous black line in (b). Vertical dashed blue lines delimit solar cycles 23 and 24. The colored blocks represent the phases of the solar cycles. The period now is from 1995-08-05 to 2019-05-29.

Table 4.1: Statistical information from Figure 4.3a for γ. These are the mean, median, minimum (Min.), maximum (Max.), and 25–75 % percentiles. The first panel covers the values for the entire solar wind, then the second and third panels cover the values for the solar wind classified between slow and fast wind. As in Figure 4.3, the periods are for overall data, by cycle, and by total cycle-independent phases.

		γ Exponent					
	Period(s)	**Mean**	**Median**	**Min.**	**25 %**	**75 %**	**Max.**
Unclassified	Overall	0.505	0.512	0.198	0.482	0.537	0.644
	SC23	0.498	0.505	0.198	0.467	0.537	0.644
	SC24	0.513	0.517	0.306	0.494	0.537	0.604
	Minimum	0.524	0.525	0.414	0.501	0.549	0.617
	Ascending	0.498	0.510	0.306	0.475	0.533	0.604
	Maximum	0.488	0.500	0.198	0.451	0.525	0.614
	Descending	0.507	0.511	0.271	0.486	0.537	0.644
Slow wind	Overall	0.506	0.512	0.199	0.483	0.537	0.644
	SC23	0.497	0.506	0.199	0.466	0.537	0.644
	SC24	0.513	0.517	0.307	0.493	0.537	0.604
	Minimum	0.524	0.526	0.414	0.502	0.549	0.617
	Ascending	0.498	0.509	0.307	0.475	0.533	0.604
	Maximum	0.489	0.501	0.199	0.453	0.527	0.614
	Descending	0.508	0.512	0.271	0.490	0.539	0.644
Fast wind	Overall	0.504	0.510	0.198	0.480	0.537	0.640
	SC23	0.498	0.504	0.198	0.471	0.535	0.640
	SC24	0.511	0.516	0.306	0.495	0.537	0.601
	Minimum	0.522	0.523	0.427	0.497	0.551	0.615
	Ascending	0.500	0.512	0.306	0.474	0.533	0.601
	Maximum	0.481	0.495	0.198	0.442	0.520	0.596
	Descending	0.504	0.508	0.272	0.481	0.534	0.640

Table 4.2: Statistical information from Figure 4.3b for D. These are the mean, median, minimum (Min.), maximum (Max.), and 25–75 % percentiles. The first panel covers the values for the entire solar wind, then the second and third panels cover the values for the solar wind classified between slow and fast wind. As in Figure 4.3, the periods are for overall data, by cycle, and by total cycle-independent phases.

			D **Divergence**				
	Period(s)	**Mean**	**Median**	**Min.**	**25 %**	**75 %**	**Max.**
Unclassified	Overall	0.0111	0.0094	1.7×10^{-5}	0.0062	0.0140	0.0458
	SC23	0.0121	0.0102	2.7×10^{-4}	0.0062	0.0164	0.0457
	SC24	0.0104	0.0092	1.7×10^{-5}	0.0066	0.0124	0.0439
	Minimum	0.0081	0.0074	2.1×10^{-4}	0.0052	0.0104	0.0215
	Ascending	0.0129	0.0110	1.7×10^{-5}	0.0073	0.0171	0.0458
	Maximum	0.0141	0.0124	9.6×10^{-4}	0.0079	0.0179	0.0439
	Descending	0.0106	0.0095	2.7×10^{-4}	0.0063	0.0130	0.0419
Slow wind	Overall	0.0112	0.0095	6.7×10^{-5}	0.0064	0.0142	0.0447
	SC23	0.0125	0.0107	3.0×10^{-4}	0.0065	0.0168	0.0447
	SC24	0.0105	0.0091	1.7×10^{-4}	0.0065	0.0125	0.0439
	Minimum	0.0083	0.0077	2.1×10^{-4}	0.0054	0.0108	0.0215
	Ascending	0.0127	0.0110	1.7×10^{-4}	0.0073	0.0168	0.0447
	Maximum	0.0142	0.0124	9.6×10^{-4}	0.0079	0.0182	0.0439
	Descending	0.0107	0.0094	3.0×10^{-4}	0.0063	0.0130	0.0419
Fast wind	Overall	0.0105	0.0090	1.7×10^{-5}	0.0059	0.0134	0.0458
	SC23	0.0111	0.0092	2.7×10^{-4}	0.0055	0.0148	0.0458
	SC24	0.0100	0.0093	1.7×10^{-5}	0.0069	0.0119	0.0364
	Minimum	0.0071	0.0066	5.1×10^{-4}	0.0046	0.0086	0.0211
	Ascending	0.0136	0.0109	1.7×10^{-5}	0.0071	0.0189	0.0458
	Maximum	0.0135	0.0121	1.9×10^{-3}	0.0076	0.0171	0.0388
	Descending	0.0105	0.0096	2.7×10^{-4}	0.0061	0.0132	0.0415

Table 4.3: Pearson correlation coefficients and p-values from the curves contrasted in Figure 4.4. The first column indicates the period, where "min", "asc", "max" and "des" denotes the phase (minimum, ascending, maximum, descending) corresponding to the cycle indicated by its subindex. The second and fourth columns show the correlation coefficients between the S_n index with γ-exponent and D-divergence. Then the third and last columns display the p-values related to correlation coefficients of S_n with γ and D, respectively.

Period	S_n **vs.** γ	p	S_n **vs.** D	p
Overall	-0.72	< 0.001	0.59	< 0.001
SC23	-0.76	< 0.001	0.62	< 0.001
SC24	-0.44	< 0.001	0.27	< 0.001
min_{23}	-0.88	< 0.001	0.91	< 0.001
asc_{23}	0.13	< 0.001	0.41	< 0.001
max_{23}	-0.25	< 0.001	0.57	< 0.001
des_{23}	-0.68	< 0.001	0.05	0.07
min_{23-24}	-0.56	< 0.001	-0.38	< 0.001
asc_{24}	-0.62	< 0.001	-0.29	< 0.001
max_{24}	0.72	< 0.001	-0.66	< 0.001
des_{24}	0.30	< 0.001	0.59	< 0.001
min_{24}	-0.85	< 0.001	-0.76	< 0.001

Table 4.4: Pearson correlation coefficients and p-values from the curves contrasted in Figure 4.5. The first column indicates the period, where "min", "asc", "max" and "des" denotes the phase (minimum, ascending, maximum, descending) corresponding to the cycle indicated by its subindex. The second and fourth columns show the correlation coefficients between the v_p solar wind speed with γ-exponent and D-divergence. Then the third and last columns display the p-values related to correlation coefficients of v_p with γ and D, respectively.

Period	v_p **vs.** γ	p	v_p **vs.** D	p
Overall	-0.21	< 0.001	-0.08	< 0.001
SC23	-0.02	0.17	-0.20	< 0.001
SC24	-0.11	< 0.001	-0.33	< 0.001
min_{23}	0.87	< 0.001	-0.97	< 0.001
asc_{23}	0.28	< 0.001	0.39	< 0.001
max_{23}	-0.14	< 0.001	-0.71	< 0.001
des_{23}	-0.60	< 0.001	-0.05	0.06
min_{23-24}	-0.67	< 0.001	-0.95	< 0.001
asc_{24}	-0.46	< 0.001	-0.21	< 0.001
max_{24}	0.10	< 0.01	-0.03	0.44
des_{24}	-0.01	0.76	0.24	< 0.001
min_{24}	-0.74	< 0.001	-0.81	< 0.001

Chapter 5

Blazars

In one of the first approaches to astrophysical systems through the use of Horizontal Visibility Graph (HVG), we have shown that this method is able to detect differences in particle velocity distributions in plasma simulations [20] (see Chapter 3). Moreover, the HVG has proved to be a robust method to characterize the solar wind plasma and has been used to study turbulent magnetic field [105], velocity fluctuations [19] and light curves of pulsating variable stars [106]. Being the closest star to Earth, the Sun and the solar wind are arguably the most studied astrophysical systems, corresponding to a valuable laboratory of natural plasma physics. During the last decades, several space missions have been launched and surveyed the space environment, making many discoveries. In contrast, the study of distant objects, such as blazars, has comparatively fewer high-quality datasets available.

Angel and Stockman [107] indicated that the word blazar was proposed by Edward A. Spiegel in the Pittsburgh Conference on BL Lac Objects in 1978, which is a combination of BL Lacertae object and quasar. Blazars are a particular type of active galactic nuclei (AGN). Emission within an AGN is produced by the accretion of matter from a black hole at its center, where the surrounding material forms an accretion disk that is heated by the dissipation of gravitational energy, generating

in some cases the expulsion of matter and energy in relativistic jets. An AGN is powered by the conversion of gravitational potential energy into radiation, although the rotational kinetic energy of the black hole can also serve as an important energy source; moreover, plasma jets are formed when the black hole rotates and the accretion disk is strongly magnetized [29]. The above details comprise what we can consider the main idea of the unified model of an AGN. This model accounts for observational differences among AGN, which are due to the different orientations of the objects as seen from Earth and the different accretion rates and masses of the central black holes [30]. Observations show that a blazar is an AGN with a jet of matter moving at relativistic velocities oriented near our line of sight. Blazars are the most violent AGN, emitting predominantly non-thermal radiation with strong variability across the electromagnetic spectrum [29], from the radio band to extremely high gamma-ray energies on time scales that can be as short as minutes. Among blazars, we can distinguish BL Lacertae (BL Lac) objects, which have weak emission lines or a featureless continuum in the optical spectrum, and flat-spectrum radio quasars (FSRQ), which have prominent emission lines in the optical spectrum.

The variability of blazars can be observed in different energy bands. To investigate the physical mechanisms that generate the observed variations in blazar light curves, many studies have been carried out at various wavelengths. Some techniques work from the frequency domain and others work from the time domain. The main tool of analysis to use in different bands is to determine their Power Spectral Densities (PSD) [108], since the PSD can provide clues about the mechanism driving the variability. For instance, Max-Moerbeck et al. [109] have modeled light curves as red noise processes with the PSD to model the variability and to set constraints on the statistical significance of interband correlations. In addition, light curves and PSDs have

been investigated with several other methods. Gaussian Process (GP) is especially useful for analyzing astronomical time-series data, and there are even studies that have initiated more active methodological discussion on multiband time-series data by implementing multi-output GP [110]. In Tarnopolski et al. [111], the toolset includes Lomb-Scargle Periodogram (LSP) [112], wavelet scalogram [113], Autoregressive Moving Average process (ARMA) [114], Continuous-time ARMA (CARMA) [114], the Hurst exponent (H) [115] and others. In fact, an algebraic relationship between the H-exponent of the time series and the exponent of the power-law degree distribution of the visibility graph (non-horizontal) has been obtained. It has been shown that the exponent of the power-law degree distribution depends linearly on H [116]. H measures the statistical auto-similarity of a time series, i.e., the long-range dependence or memory of a process. Small-scale studies have been made to classify light curves with the H, where it has been found that two FSRQs and four BL Lac exhibit long-term memory in the underlying process governing the optical variability of 44 identified blazar candidates [115]. The overall challenge is to apply effective techniques to model the complex nature of light curve variations that occur in different bands and time scales.

We have started a study of the variability properties in the radio band of blazars observed with a large-scale, fast cadence 15 GHz radio monitoring program with the Owens Valley Radio Observatory (OVRO) 40 m Telescope that has produced 12 years of data for over 1800 sources observed twice a week [117]. Thus, this set of time series corresponds to the most comprehensive study of blazar variability in the radio band available at this time and is ideal for conducting our study, presenting a new perspective on the methods commonly used to study AGN. We focus on characterizing the high-energy emission mechanisms of blazars by analyzing the variability

in the radio band of the light curves of more than a thousand sources. We seek to describe the light curves, i.e., to analyze the observed flux density as a function of time of these sources as a first approximation of the complexity parameters in active galactic nuclei. We are interested in assigning degrees of stochasticity to blazars, modeling the time series of light curves as complex networks. For this purpose, we rely on visibility algorithms that convert time series into graphs [7], which offers another perspective for the study of variability in light curves.

In this part of the thesis, we map time series of the light curves with the Horizontal Visibility Graph algorithm. Thus, we measure the characteristic exponent to describe their stochasticity (Section 2.2), and the Kullback-Leibler Divergence to describe their irreversibility (Section 2.3). These metrics, which guide the analysis of our study, are obtained this time in order to detect a different behavior of the blazar light curves. We will analyze if the properties of degrees distributions are related to the spectral classification of blazars, and we are interested in contrasting with a common measurement of variability in light curves, the excess variance. To the best of our knowledge, this is the first approach to the study of blazars using HVG, which manages to identify different ranges of the KLD for different astronomical sources. The chapter is organized as follows. Section 5.1 explains technical details about these radio observations and shows a sample of a light curve to illustrate the characteristics of data series used by this study. Section 5.2 exposes our results after applying the method on all available blazar light curves.

5.1. Blazar light curves

The blazar subclasses, BL Lac and FSRQ, are defined by the properties of their optical spectra. The spectra of FSRQs show broad emission lines, while BL Lacs

show very weak or no emission lines [29, 118]. Other properties of the sources are also correlated with the subclasses as described in the references above. In this thesis, we focus on working with observational data of blazars in the radio band.

The OVRO data were obtained from the OVRO 40 m Telescope Monitoring Program [117]. The telescope uses off-axis dual-beam optics in which the beamwidth (FWHM) is 157 arc seconds. The cryogenic receiver uses a HEMT amplifier and is centered at 15 GHz with 2 GHz equivalent noise bandwidth. Gain fluctuations and atmospheric and ground contributions are removed with the double-switching technique where one of the beams is always pointed at the source. Details of the observation and data reduction [117] cover the absolute calibration and the uncertainties, which include both the thermal fluctuations in the receiver and systematic errors that have been added under a rigorous procedure [117].

It is important to study the amplitude of variability in AGN light curves. The importance of variability lies in the fact that, being a fundamental property of blazars, it can be used as a tool to distinguish them from other astrophysical objects [115]. One of the quantities most commonly used to estimate this property is the excess variance. According to Turner et al. [119], the normalized excess variance is

$$(\sigma_{\rm rms}^{\rm norm})^2 = \frac{1}{n\mu^2}\sum_{i=1}^{n}\left[(X_i-\mu)^2-\sigma_i^2\right], \tag{5.1}$$

designating the flux density for the n points in each light curve as X_i, with its arithmetic mean μ and errors σ_i. The excess variance is useful for comparing the variability in different light curves. As a first application of complex networks to radio light curves, we use $\sigma_{\rm rms}^{\rm norm}$ to contrast with measures that also distinguish the amplitude of the light curve variability, now according to its visibility (explained in Section 2). Note that we use the square root of the excess variance, which is

also known as the fractional root mean square variability amplitude [120, 121]. Both quantities give us the same information, but the last one is a linear statistic that gives the root mean square variability amplitude in percentage terms [108].

If we want to compare our complexity parameters with the intrinsic properties of the blazar sources, we must consider its anisotropy and associated relativistic effects in the flux measurement. There are astrophysical objects such as stars, that can be regarded as spherically symmetric and therefore isotropic emitters. The isotropic luminosity is simply $L^i_\nu = 4\pi F_\nu d_L^2$, where F_ν is the flux density, d_L the luminosity distance which is related to redshift and is computed assuming a ΛCDM model [122]. However, AGN are not isotropic emitters. The flux of a blazar depends on the viewing angle (see Figure 5.1, because the source emits different amounts of energy depending on the direction of the relativistic jet. Also, to express the flux in the emitting frame, $F^{\rm em}$ evaluated at the observed frequency, the transformation between fluxes perceived in the emission's frame and observer's frame has the form $F^{\rm rec}_{\nu^{\rm rec}} = F^{\rm em}_{\nu^{\rm rec}}\delta^{3+\alpha}$, with δ the Doppler factor. A Lorentz boosting factor of $\delta^{3+\alpha}$ for a power-law radiation spectrum $F_\nu \propto \nu^{-\alpha}$ results when comparing the fluxes at the same frequency in both frames [123]. Then, with these two corrections to the isotropic luminosity and integrating from the source in the two orientations of the jet, the following is obtained

$$L_\nu = 4\pi d_L^2 F^{\rm rec}_{\nu^{\rm rec}} \delta^{-(3+\alpha)} \int_0^{\pi/2} e^{\frac{-\left(\theta^2-\theta_{\rm v}^2\right)}{2\theta_{\rm op}^2}} \sin\theta d\theta\,, \tag{5.2}$$

where $\theta_{\rm op}$ is the intrinsic opening angle of the jet lobe, and $\theta_{\rm v}$ is the viewing angle, as illustrated in Figure 5.1. The jet opening angle can largely influence the observed jet emission [124].

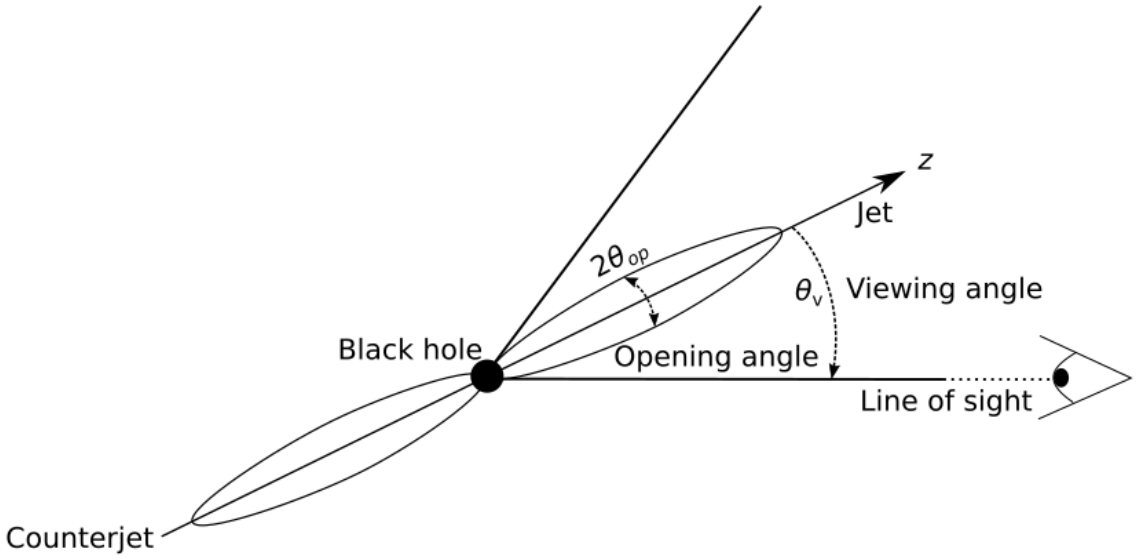

Figure 5.1: A simple model of a blazar. The model includes a jet and a symmetric counterjet. The jet is characterized by an opening angle and a viewing angle to the line of sight to the observer. This anisotropy needs to be considered to properly derive the intrinsic luminosity.

5.2. Results

We analyze the physical properties that could be conditioning the behavior of the light curves using DHVG and UHVG. Initially, we work with a data set that contains 1298 sources, where 400 are BL Lac and 898 are FSRQ. The optical classes are taken from the Roma BZCAT Multi-Frequency Catalog of Blazars 5th edition. The Multi-Frequency Catalogue of Blazars is one of the most complete lists of Active Galactic Nuclei whose emission properties are recognized as typical of blazars. It includes the list of sources and an essential compilation of multifrequency data from radio to gamma rays [125].

We applied the HVG algorithm to the time series of the light curves of blazars finding an exponential behavior on the degree probability distributions in most light curves, as shown in Figure 5.2 for both methods UHVG (black dots) and DHVG

(color solid lines). Once we calculate the degree probability distribution $P(k)$ of the UHVG, we proceed to compute the critical exponent γ as the slope of the semilog plot with the method of least squares in a range from $k = 3$ to some k with the lowest probability, without including it and avoiding the low probability floor in the heavy tails (see Figure 5.2b in Section 5.2). When making this adjustment, we find that some degree probability distributions did not fit an exponential, so we discarded those light curves.

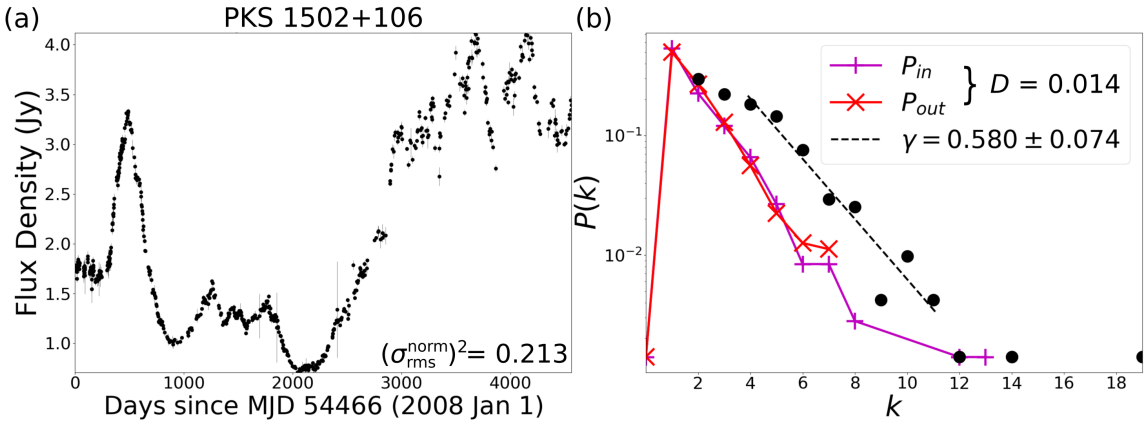

Figure 5.2: (a) Example radio light curve for the blazar PKS 1502+106 [126], a FSRQ source. (b) Semilog plot of degree distributions from DHVG, P_{in} in magenta and P_{out} in red, and from UHVG, P in black dots with their fit on the dashed line. The value of the normalized excess variance $(\sigma_{\text{rms}}^{\text{norm}})^2$ of the light curve, D, from the distance between degree distributions **ingoing** and **outgoing**, and γ, from the exponential behavior $P(k) \sim \mathrm{e}^{-\gamma k}$, are shown.

As from the fit for the slope in the semilog plots for $P(k)$ required to obtain the γ-exponent from the exponential form $P(k) \sim \mathrm{e}^{-\gamma k}$ (described in Section 2.2), we proceeded to select source by source such that its degree distribution was represented in this exponential behavior. Figures 5.3 and 5.4 show six of the 843 selected FSRQ sources, and six of the 380 selected BL Lac sources, respectively. Figures 5.5 and 5.6 show six of the 55 discarded FSRQ sources, and six of the 20 discarded BL Lac sour-

ces, respectively, in which some characteristics escape from the adequate behavior to assign a representative γ value to the curve. Thus, just 5 % of BL Lac and 6.1 % of FSRQ are discarded because they deviate from the exponential model being fit. We are still left with 843 FSRQ and 380 BL Lac sources.

Now, having the degree distributions well-adjusted for each light curve, we have the critical exponent γ (UHVG) per source and we plot the PDF for these data sets, as is shown in Figure 5.7a. The statistical detail of those PDFs analyses is in Table 5.1. Figure 5.7a shows a clear difference between the light curves of BL Lac and the FSRQ. With a dotted line, we mark the limit proposed by Lacasa and Toral [16] between stochastic time series and chaos for the UHVG analysis. From Figure 5.7a, we observe when plotting the PDFs that the PDF curves separate around this limit. That is, the BL Lac sources have a peak of the γ PDF on the left of the dotted line, with $\gamma = 0.392$, whereas the FSRQ sources show the peak of the γ PDF on the right of the limit $\gamma_{\text{un}} \approx 0.405$, with $\gamma = 0.446$. Thus, following Reference [**?**], most BL Lac light curves show a chaotic behavior, while most FSRQ light curves show a time series with a correlated stochastic behavior.

As a second analysis, we calculate the KLD using the technique explained in Section 2.3. The results obtained for D correspond to a smoother weighting of the original values. So, it is possible to analyze cases of high irreversibility without necessarily assigning an infinity. Figure 5.7b shows the PDF for the value of D, which is a measure of the irreversibility of the time series. In this case, both classes of light curves show the same behavior of this parameter, low values of D between 10^{-3} and 10^{-1} as is shown in Table 5.2, but the peaks of these PDF do not show a difference between BL Lac and FSRQ.

As complementary analysis to the usual calculation of the KLD, we also calculate

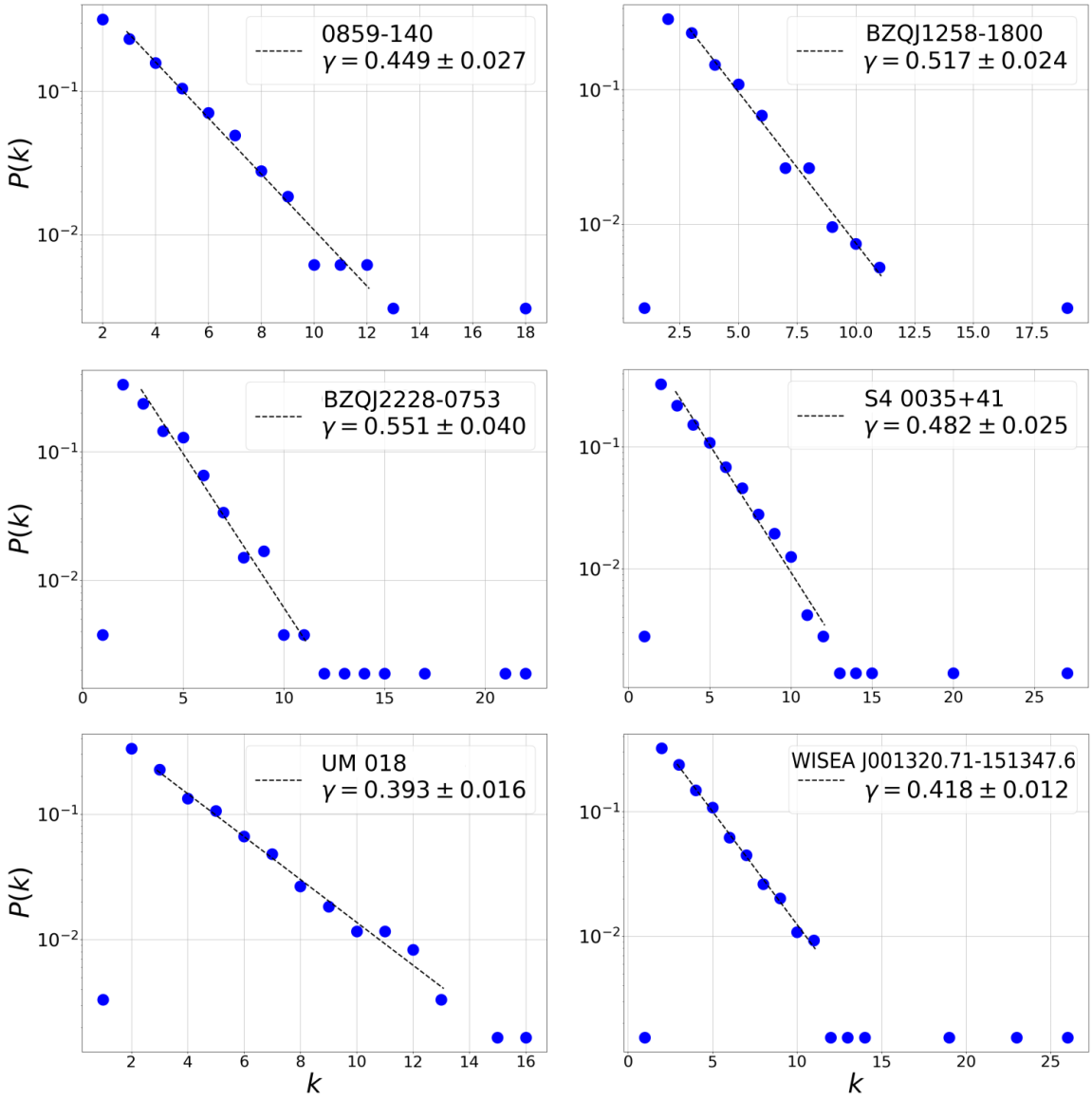

Figure 5.3: Examples of selected probability distribution fits to FSRQ light curves. Degree distributions $P(k)$ in blue dots with their fit with a dashed black line.

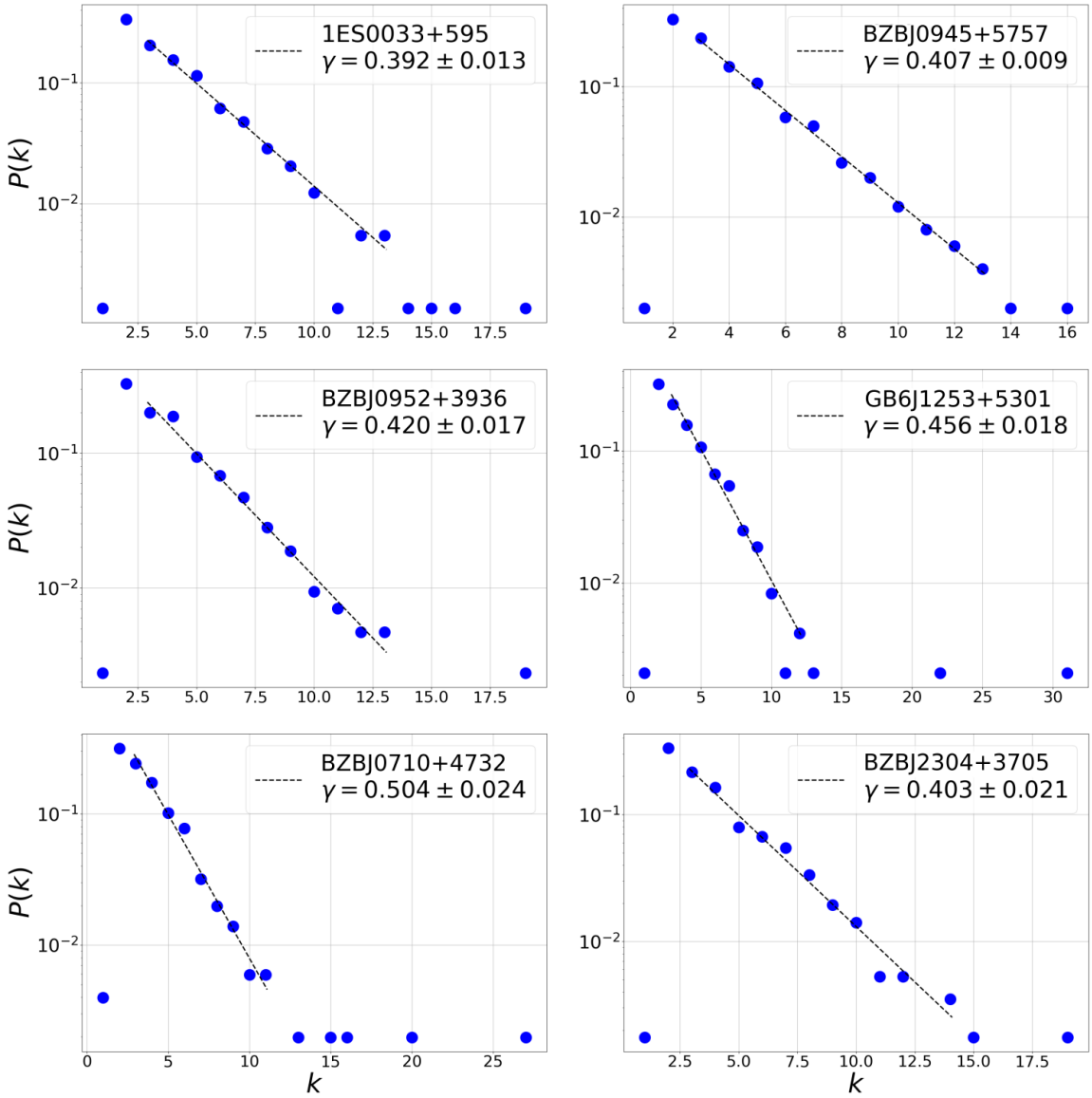

Figure 5.4: Examples of selected probability distribution fits to BL Lac light curves. Degree distributions $P(k)$ in blue dots with their fit with a dashed black line.

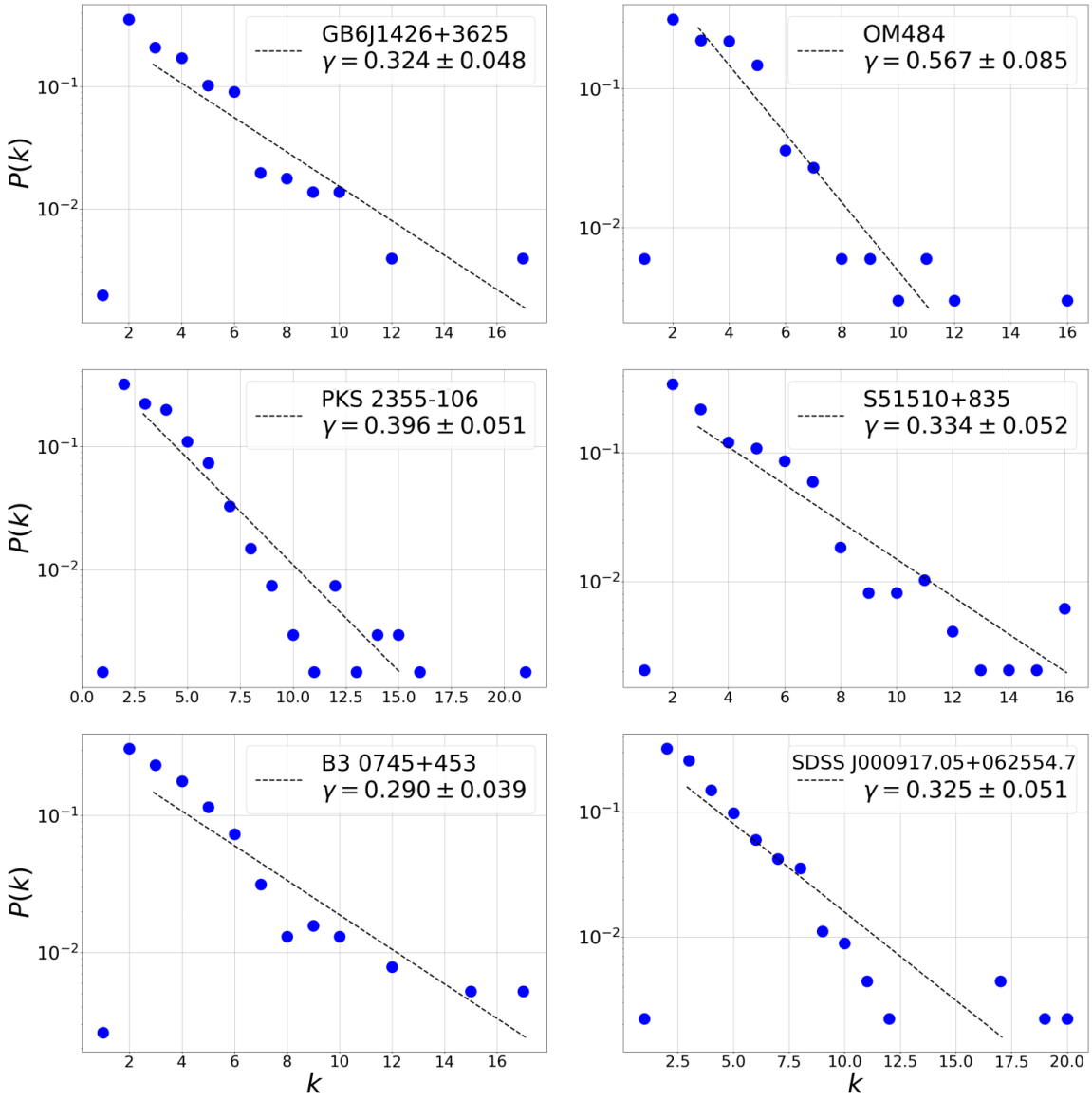

Figure 5.5: Examples of discarded probability distribution fits for FSRQ light curves. Degree distributions $P(k)$ in blue dots with their fit with a dashed black line.

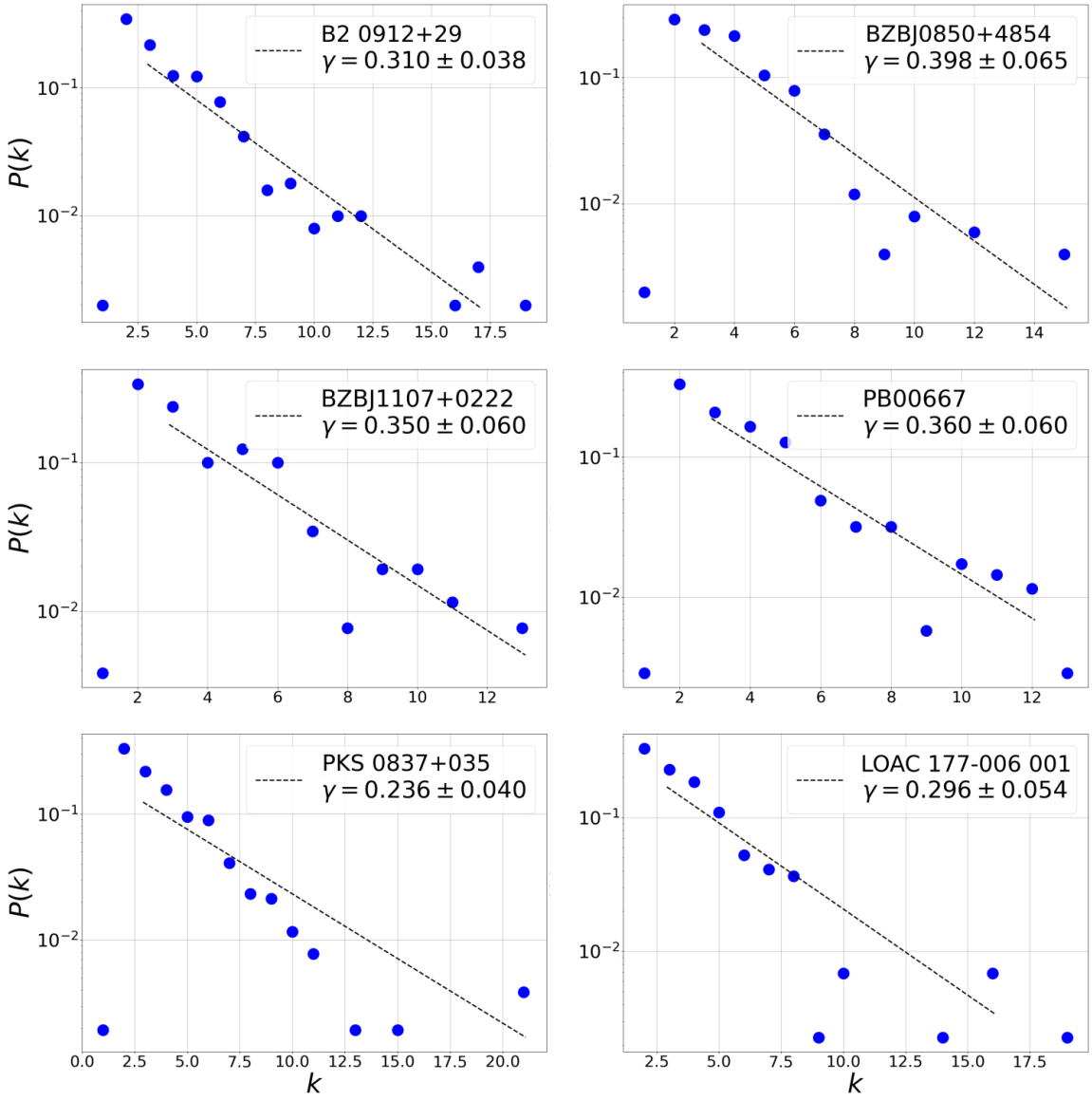

Figure 5.6: Examples of discarded probability distribution fits for BL Lac light curves. Degree distributions $P(k)$ in blue dots with their fit with a dashed black line.

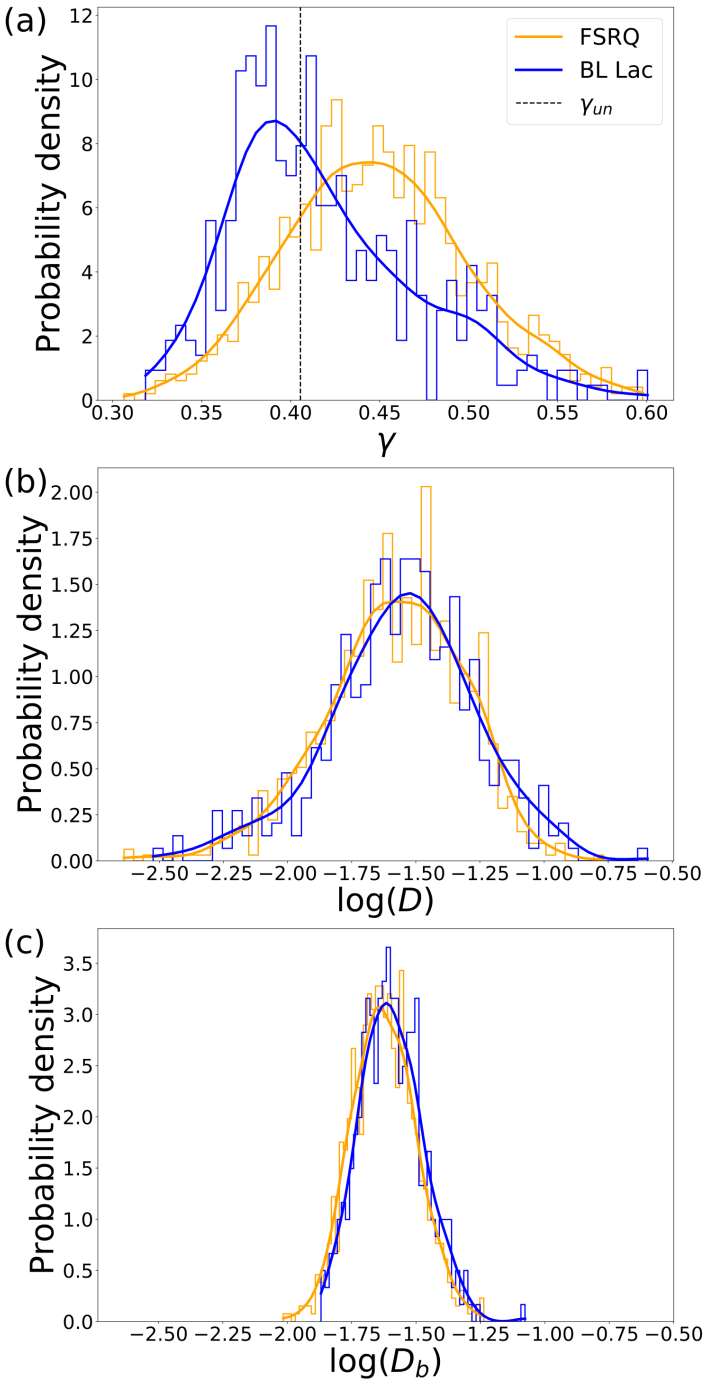

Figure 5.7: Probability density function (PDF) of (a) γ, (b) $\log(D)$, and (c) $\log(D_b)$ values for the different subclasses of blazars. Yellow for FSRQ and blue for BL Lac. There are 843 FSRQ and 380 BL Lac sources. With the dotted line in (a), we mark the limit $\gamma_{\rm un} \approx 0.405$ between correlated stochastic and chaotic time series [16].

our statistical measure KLD from the bootstrap resampling technique [127], whose purpose is to take into account the observational uncertainty inherent in the data and non-uniform sampling. The bootstrapping basically consists of having a parent data sample $\mathbf{Y}= \{Y_i\}_{i=1,...,m}$ of m elements, we generate bootstrap samples $\mathbf{Y}^*$ by extracting m elements with random replacement from the parent list, keeping their temporal occurrence. In our case, we perform this process 1000 times, in which we compute the KLD for each bootstrap sample (using the smoothing technique explained in Section 2.3). Then, we choose the median of this process, D_b. Thus, Figure 5.7c shows the PDF for the value of D_b. As in Figure 5.7b, both classes of light curves show the same behavior for the bootstrap KLD. There are much lower values of D_b since they are now on the order of 10^{-2} as shown in Table 5.3, without yet finding much difference between BL Lac and FSRQ. This reiterates what was obtained from the original time series in Figure 5.7b.

Table 5.1: Statistical information on the γ values from Figure 5.7a, i.e., the peaks of PDFs, the mean, median, standard deviation, minimum and maximum values, and the 25 % and 75 % percentiles of the sample.

			γ **Exponent**					
Class	**peak**	**mean**	**median**	**std**	**min**	**25 %**	**75 %**	**max**
FSRQ	0.446	0.449	0.447	0.052	0.306	0.413	0.482	0.598
BL Lac	0.392	0.419	0.409	0.053	0.319	0.381	0.451	0.600

Table 5.2: Statistical information on the D values from Figure 5.7b, i.e., the peaks of PDFs, the mean, median, standard deviation, minimum and maximum values, and the 25 % and 75 % percentiles of the sample.

			D **Divergence**					
Class	**peak**	**mean**	**median**	**std**	**min**	**25 %**	**75 %**	**max**
FSRQ	0.026	0.031	0.027	0.019	0.002	0.018	0.041	0.170
BL Lac	0.030	0.034	0.029	0.025	0.003	0.019	0.043	0.253

Table 5.3: Statistical information on the D_b values from Figure 5.7c, i.e., the peaks of PDFs, the mean, median, standard deviation, minimum and maximum values, and the 25 % and 75 % percentiles of the sample.

			D_b Divergence					
Class	**peak**	**mean**	**median**	**std**	**min**	**25 %**	**75 %**	**max**
FSRQ	0.023	0.025	0.023	0.007	0.010	0.019	0.029	0.058
BL Lac	0.024	0.026	0.025	0.008	0.014	0.021	0.031	0.084

In order to find possible correlations between parameters of the complex network extracted from these time series and a physical measure of variability in AGN, we compare the values of $\sigma_{\text{rms}}^{\text{norm}}$ (from Equation 5.1), that is the square root of the normalized excess variance [119], with the critical exponent γ in Figure 5.8a and with the divergences D and D_b in Figures 5.8b–c, which are all dimensionless quantities.

From the previously selected sources, we found using NASA/IPAC Extragalactic Database (NED)[1] the redshift of 88 BL Lac and 829 FSRQ sources, so we calculate the luminosity distance (with the cosmological parameters given in Aghanim et al. [122]). Also, we use the median of the flux density of the radio light curves under study, because a large flare moves the mean a lot, but does not significantly affect the median. Given all this, we calculate the isotropic radio luminosity, L_ν^i, as shown in Figures 5.9a–c. Next, as preliminary results to contrast our complexity parameters with the corrected luminosity in the radio band, L_ν, we use the MOJAVE-XIV survey by Pushkarev et al. [128]. This catalog, which is provided by the Monitoring of Jets in Active Galactic Nuclei with the VLBA Experiments (MOJAVE) project, collects the largest number of sources to which the Doppler factor, and viewing and intrinsic opening angles are reported. Thus, we calculate the luminosity emitted by the jet considering the corrections described by Equation 5.2. The

[1] https://ned.ipac.caltech.edu

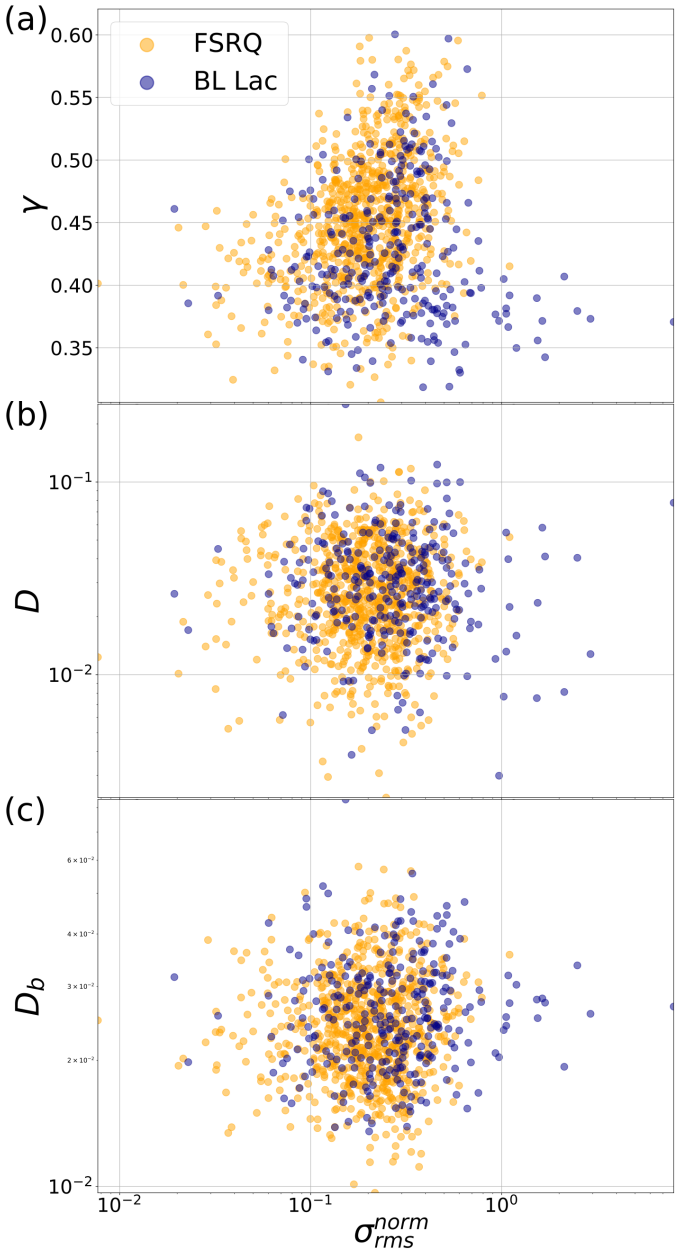

Figure 5.8: Scatter plots of square root of the normalized excess variance vs. (a) γ, (b) D, and (c) D_b. Yellow for FSRQ and blue for BL Lac. There are 843 FSRQ and 380 BL Lac sources.

spectral indexes of the jet cores are similar between the BL Lac and FSRQ optical classes of the MOJAVE program sample sources, and on average are close to being flat, specifically $\alpha_{\rm core} = 0.22 \pm 0.03$ [129]. In our study for some simplification and understanding that we do not have the spectral index for all remaining sources, we use $\alpha = 0$. These results are shown in Figures 5.9d–f.

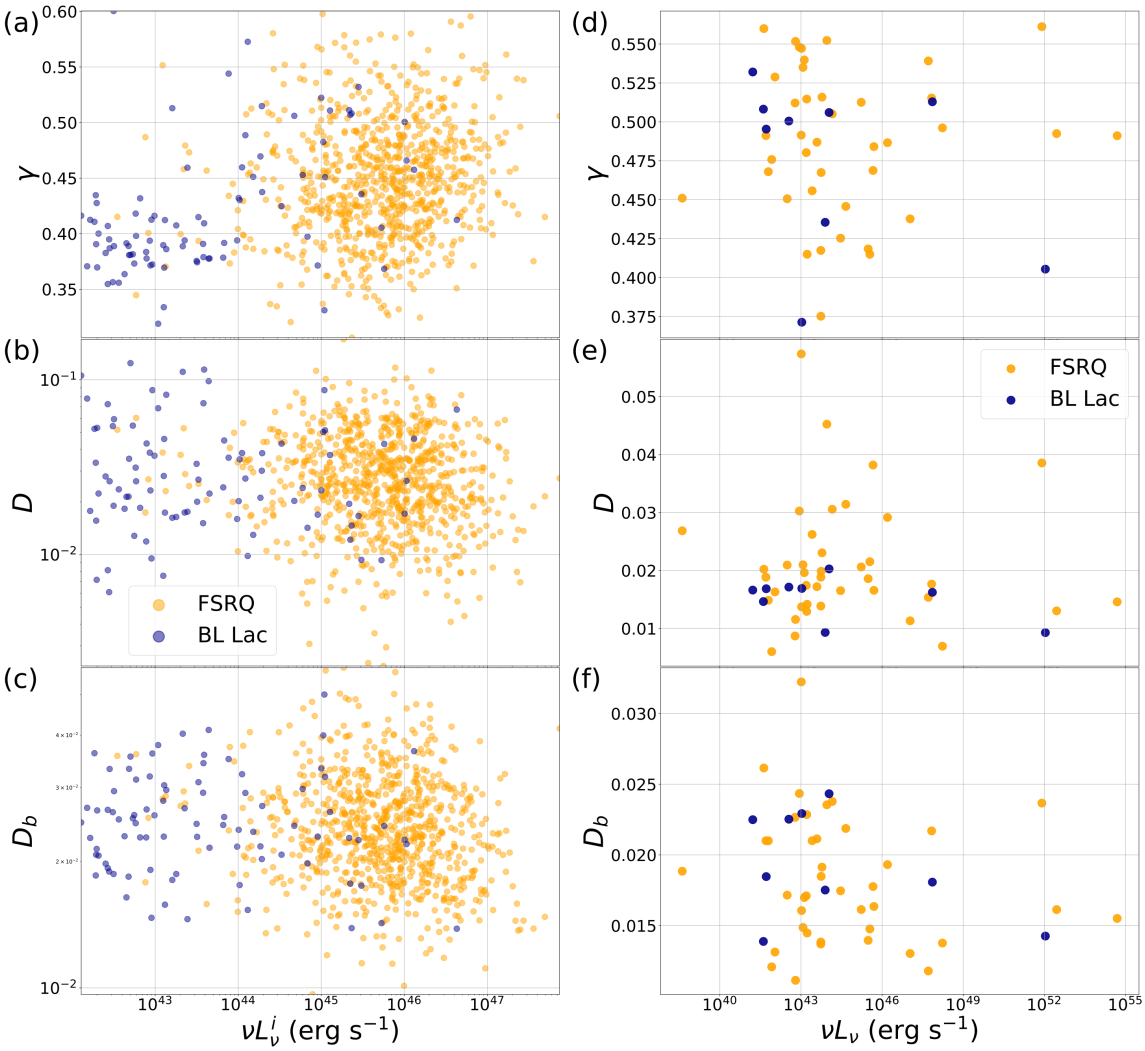

Figure 5.9: Scatter plots of (left) isotropic radio luminosity and (right) corrected radio luminosity vs. (a, d) γ, (b, e) D, and (c, f) D_b. The left panel shows 829 FSRQ and 88 BL Lac sources, while the right panel shows 40 FSRQ and 9 BL Lac sources.

We note that Figure 5.9 generally shows a large scatter in the values for the values of γ and D (with Pearson correlation coefficients between -0.10 and 0.11, without considering spectral classification), suggesting independence of the isotropic luminosity. However, in the left panel, γ shows slightly less scatter relative to L^i_ν, especially for BL Lac sources that have a Pearson correlation coefficient of 0.45 and a p-value of less than 0.001. Although this is not a new fact, since from the histograms we already saw that it can differentiate between spectral classes. Referring to the results obtained for the corrected luminosity L_ν in the right panel of the Figure 5.9, there are still too few points for a robust statistical behavior to be established. The reason there are fewer dots in the right panel is because there are still few sources for which their jet parameters are known.

One might think that if there is a linear relationship between both luminosities, we could compensate for the missing information from the sources and thus not lose the consistency of the statistics. But Figure 5.10 shows the independence of both magnitudes, which would not allow transforming the isotropic to the corrected one so directly. Thus, knowing the viewing and opening angles, the redshift, the Doppler factor, and even the spectral index, is relevant for a proper search of intercorrelations.

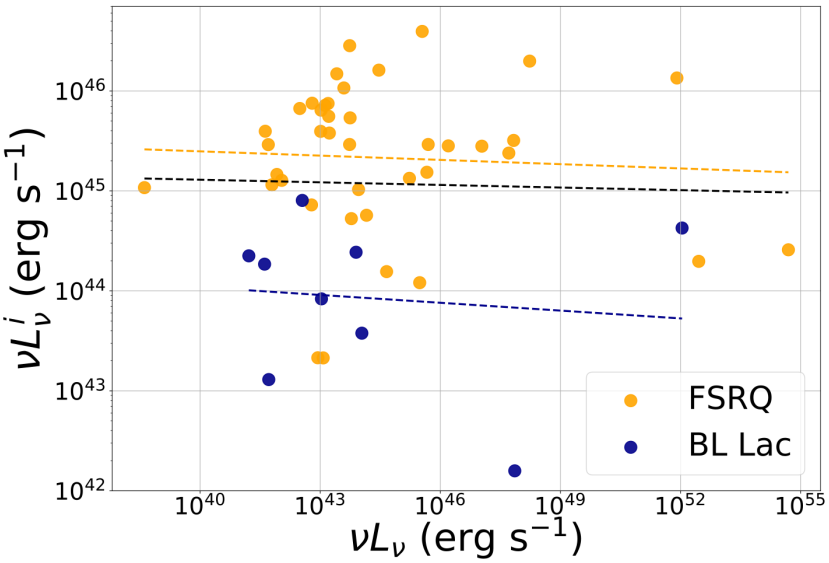

Figure 5.10: Scatter plot for corrected radio luminosity νL_ν vs. isotropic radio luminosity νL^i_ν(at 15 GHz). The log-log fits are: for all sources without considering spectral classification (dashed black line): $y = -0.009x + 45.460$, for BL Lac sources (dashed blue line): $y = -0.026x + 45.080$, for FSRQ sources (dashed yellow line): $y = -0.014x + 45.965$. Results with p-values greater than 0.6.

Chapter 6

Discussions and Conclusions

We have extended the limits of the applications of the Horizontal Visibility Graph method by dealing with time series of plasma simulations and with two astrophysical systems: solar wind and blazars. Each system involved different challenges to be faced. From the HVG model, we derived degree distributions that give information about time correlations, from which we calculate two important parameters: the critical exponent, γ, and the Kullback-Leibler divergence, D. As D moves away from $D = 0$, the physical mechanism generating the time series moves away from reversibility and we are in the presence of a dissipative system; γ allows us to discriminate between correlated stochastic or uncorrelated chaotic time series in relation to the limit value $\gamma_{\text{un}} \approx 0.405$ proposed by Lacasa and Toral [16].

Below, we will summarize the discussions on each system individually: PIC simulations, solar wind and blazars. And finally, we conclude this thesis as a whole.

6.1. Discussion of PIC simulations results

In this study we have modeled a turbulent plasma as a complex network, applying the method known as Horizontal Visibility Graph to study the reversibility on magnetic fluctuations. We have developed algorithms to build HVGs from magnetic field

fluctuations time series obtained from PIC simulations of collisionless magnetized plasmas. We have analyzed three cases for the time series: a time series of a plasma far from the thermodynamic equilibrium ($\kappa_e = 3$), a time series closer to the thermodynamic equilibrium ($\kappa_e = 15$), and a Maxwell-Boltzmann distribution, representing a plasma in thermal equilibrium. For these three time series, we have computed the degree distribution of the connectivity, which gives information associated with the time correlations in the distribution, and the KLD, which provides information related to the reversibility of the time series.

In the case of the degree probability distribution:

1. We have found an exponential behavior for all cases analyzed, i.e, short-range correlations for all time series (Kappa and Maxwell-Boltzmann distributions). Our results show that the decaying critical exponent γ is the largest for the Maxwellian-Boltzmann distribution, and decreases with decreasing kappa value. Moreover, for $\kappa_e = 3$ the critical exponent is closer to the limit value $\gamma_{\text{un}} = \ln(3/2)$ in which the time series becomes uncorrelated, being chaotic for smaller values ($\gamma < \gamma_{\text{un}}$). These results suggest a lower time correlation for $\kappa_e = 3$ than the Maxwell-Boltzmann distribution, which is consistent with the fact that in collisionless plasmas out of thermodynamic equilibrium long-range interactions dominate [58]. As already mentioned, in all cases our simulations correspond to isotropic plasmas that are steady-state solutions of the Vlasov equation. Thus, the electromagnetic fluctuations correspond to spontaneous emissions of a system composed of discrete charged particles in random motion. Consequently, the fluctuations provide information about the smallest scales where fast short-range interactions dominate. In the case of a plasma system these scales are strongly related to the Debye length λ_D.

2. Inside the Debye sphere (a sphere of radius λ_D) particles interact individually, and outside the Debye sphere, long-range collective interactions dominate. This is directly related to the correlations between the particles that produce the magnetic fluctuations, which depend on the shape of the velocity distribution function. In the case of Kappa distributions the Debye length of the plasma is a decreasing function of κ that collapses to zero for $\kappa = 3/2$ [130]. Therefore, in plasmas described by a Kappa VDF, the short-range correlations are less effective since the Debye length is smaller. Outside the Debye sphere the thermal energy dominates the potential energy and the correlations are practically dissolved [51]. In contrast, since the Debye length is greater, in a Maxwellian plasma the short-range correlations dominate, as they decay faster, both temporally and spatially. Regarding our results, this is reflected in the gamma value that seems to behave as a increasing function of κ_e.

In the case of the KLD:

3. For both the original and detrended time series, we have obtained low values of the divergence D for all cases, which is consistent with plasmas in a steady state according to the Vlasov equation. However, the method has shown to be sensitive enough to distinguish higher values of irreversibility for the Kappa distribution than the Maxwell-Boltzmann case. The irreversibility associated with the Kappa distributions is related to the non-extensive nature of these distributions [131], showing an increase in the value of the KLD for decreasing values of κ.

4. The increase in the value of the KLD indicates a larger value of the entropy in the system. For Kappa distributions following the dynamics of a non-collisional

plasma, particles lose individuality and interact collectively increasing the entropy [58]. On the other hand, the Maxwell-Boltzmann distribution shows low values for the KLD, consistent with the Gibbs-Boltzmann entropy. The Maxwell-Boltzmann distribution is related to low values of entropy, in contrast to non-thermal Kappa distributions where it is possible to find a higher (non-extensive) entropy, associated to electromagnetic long-range interactions that dominate the dynamics in the plasma.

In summary, considering only the limited information provided by the time series, our results seem to indicate a robust relation between the shape of the VDF (given by the Debye length and its dependence on κ) and the nature of the correlations dominating the magnetic field fluctuations time series represented by γ [16]. The connectivity probability distribution shows how the Kappa distribution for low values of κ tends to produce uncorrelated time series, while the Maxwell-Boltzmann distribution shows a stochastic time series behavior. Furthermore, we can see that the KLD associated to the HVG is able to distinguish the level of reversibility in the time series obtained from PIC simulations, and this reversibility seems to be associated with the thermal equilibrium in the plasma. Our results suggest a high sensitivity of the HVG algorithm and a relationship between KLD, κ, and the entropy of the system. The technique applied here has allowed us to address the role of non-thermal particles distributions in poorly collisional plasma environments.

6.2. Discussion of solar wind results

In this study, we extracted the information presented in time series of solar wind magnetic fluctuations from 1995-01-01 to 2019-12-31, approximately during the solar cycles 23 and 24, with the HVG model that establishes a geometric connection

criterion based on the variability, sequence, and precedence of each data point of the series. By calculating the time evolution of D and γ parameters, we can study the dissipative and stochastic features of the Sun by periods. We have analyzed these values as a function of solar activity (in terms of solar cycles and solar cycle phases) and solar wind speed (slow and fast solar wind).

In terms of solar activity we conclude that:

1. The HVG method detects differences in intensity between SC23 and SC24 (it can be seen in Figure 4.4). Previous studies show that SC24 had the lowest activity in terms of sunspots, even compared to the last five previous solar cycles [102]. From a general analysis between SC23 and SC24, γ-exponent reaches its minimum values in SC23 (Figure 4.3a), while D-divergence was lower for SC24. Then, the γ behavior suggests that during both solar cycles, the magnetic fluctuations of the solar wind at 1 AU from the Sun are correlated stochastic time series, not chaotic. At large scales, magnetic fluctuations have a rather Gaussian behavior regardless of the type of wind [82]. This can be observed in the model of energy transfer among scales under the Langevin equation applied by Gallo-Méndez and Moya [132], whose study agrees with that of Greco et al. [133] in that the Probability Density Function (PDF) of Partial Variance of Increments (PVI) of the magnetic fluctuations present more Gaussian distributions at the fluid scale. This Gaussian PDF of PVI is associated with Brownian motions in the solar wind, which corresponds to a properly stochastic process. Also, we realize that D indicates correlation with solar activity, and in contrast, γ-exponent indicates anti-correlation with solar activity. The anti-correlation by period between these two complexity parameters is verified in Figure 4.3c. So, this plasma has turbulent structures such that when the

physical dissipative processes are less effective at large scales, they generate more correlated stochastic magnetic fluctuations. In any case, the intercorrelations vary throughout the solar cycle (see Table 4.3) because different Sun's magnetic configurations were possible in these cycles, even during too quiet periods, and the decrease in the index S_n may differ from the evolution of the interplanetary magnetic field [102].

2. Exploring throughout solar phases, the minimum phases of each cycle coincide with the reversibility range of the KLD, and the maximum phases are recognized as larger values of KLD. Since D is a ratio between outgoing and incoming connections, when D increases, it indicates that the distribution of relative magnitudes in the data is different between their forward and backward visibility within the network, which makes the time series more irreversible. The transfer of fluctuations in the turbulent solar wind is a memoryless process, i.e. a Markovian process [134]. As greater irreversibility (Markovian processes) is observed in solar maxima, large-scale instabilities, which are understood to be the physical mechanisms responsible for the generation of turbulence, would be dominating in these periods. Thus, at minima, the fluctuations are less complex and less turbulent. In addition, the γ value seems to increase with decreasing magnetic activity in the Sun, i.e., fewer sunspots in the photosphere. This calculation means that the distribution of connections is more concentrated, i.e., a few nodes share all the connections. In summary, from Table 4.1 and 4.2, this study reveals that $\gamma_{\text{min}} > \gamma_{\text{des}} > \gamma_{\text{asc}} > \gamma_{\text{max}}$, and $D_{\text{min}} < D_{\text{des}} < D_{\text{asc}} < D_{\text{max}}$, in terms of solar phases. Thus the complexity parameters calculated here are consistent with physical behavior.

3. With the chosen time scale to calculate the complexity parameters in the study and the yearly smoothing applied, we observed that each phase contains its own peak in the value of D. This relation could provide relevant and complementary information to the sunspot number measurement and possible forecasts of the solar cycle. Namely, if a peak in D has occurred, it would be possible to estimate that the phase is coming to its end. Moreover, the fact that the minimum phases are captured by the reversibility range suggests that the series has memory at those times, which is related to non-Markovian processes. Such behavior could robustly contribute to the predictability of the onset of a solar cycle. Thus, the KLD can be useful as a statistical measure to compare behaviors toward the future with behaviors toward the past. However, more supporting information would be needed to corroborate this idea.

In addition, regarding solar wind speed, we have found that:

4. Given the classification between fast and slow wind according to the speed, the exponent γ behaves uniformly. Its variations for fast and slow solar wind concerning the general (unclassified) behavior are not at all evident (Figure 4.3a). This conclusion is in agreement with the results of Sorriso-Valvo et al. [84], in which they indicated that the intermittency (interpreted as the result of the multifractal properties of the turbulent cascade and due to the contribution non-Alfvénic structures [80]) of the magnetic field intensity was similar for the slow and fast wind. On the other hand, directed degree distributions can clearly distinguish the type of solar wind due to the KLD. From Table 4.2, the slow wind, which is more variable, is precisely the type of wind that achieves the highest values in the D-divergence, except in the ascending phase, where only

the median corroborates this and not the mean, see Figure 4.3b. Although the fast wind has generally been observed to be less intermittent than the slow wind [135] since the fast wind is more Alfvénic than the slow wind, Wawrzaszek et al. [80] surprisingly detected that the magnetic field turbulence of the slow solar wind was less intermittent at the SC23 maximum. From our results, we did not observe any peculiarity in the SC23 maximum that could support the idea of a new type of slow Alfvénic wind. However, in the ascending phases, the slow wind turned out to be less irreversible. Perhaps, this method could detect the presence of Alfvénic slow wind (with some characteristics common to the fast wind) before the maximum phases.

5. In Figure 4.5 the critical exponent and KLD have a dynamic intercorrelation throughout the cycles. However, in Table 4.4 γ does not tend to exhibit significant linearity with solar wind speed. Figure 4.5b shows an anti-correlation between the D-divergence and the solar wind proton bulk speed. This anti-correlation, according to the numbers in Table 4.4, is most significant at the minimum of each cycle, which could also allow us to estimate the start of a cycle combined with the fact that in the minimums D distinguishes better the slow solar wind from the fast solar wind.

6. The HVG technique to distinguish fast solar wind from slow wind seems more useful during solar minimum than other phases. This ability is likely because the minimum phase is when the Sun's magnetic field is more dipolar, and the solar wind structure is less complex. On the other hand, at the maximum phase, the solar wind is a particularly nonlinear combination of various solar wind types. McComas et al. [93] state that the current sheet is complex and

dynamic in itself, but around the maximum phase, highly variable solar wind fluxes are observed at all heliolatitudes, which change the configuration of the current sheet structure as a whole. Our results indicate that the slow solar wind is more dissipative than the fast wind, in terms of magnetic fluctuations, in most phases of the cycle. Further improvement in the solar wind classification procedure by considering additional parameters than just speed [80] will allow a more conclusive verification of this analysis.

In summary, our results suggest that the intercorrelations of the complexity parameters with the sunspot number index are persistent in time. They are appreciated in long periods, in this case from 1995 to 2019, or by solar cycle, and in shorter periods they are not lost either. In contrast, with the proton bulk speed, the intercorrelations are short-range in time and are only best analyzed on shorter time scales, such as solar phases. Both γ and D show larger and more statistically significant intercorrelations with sunspot number, rather than with solar wind speed. According to the observational data input and the degree distributions output through the HVG method, our results are consistent with the complex nature of solar wind turbulence at 1 AU and its relation with the complexities of the solar cycle and the Sun.

6.3. Discussion of blazar results

We have applied the method of DHVG and UHVG to a sample of 1298 light curves measured from blazars. From this analysis:

1. We find an exponential behavior on the degree probability distribution $P(k)$ for most studied sources (Figure 5.2b). We compute the critical exponent γ from the $P(k)$ in the UHVG, noting that the degree distributions are capable

of detecting differences in the spectral classification of blazars, as is shown in Figure 5.7a. In fact, the division between the peak reached by the PDF of γ for the BL Lac sources is on the left of the γ_{un} limit; meanwhile, the peak reached by the PDF of γ for the FSRQ sources is on the right of this limit. That difference suggests a chaotic behavior in the time series for the BL Lac sources and a correlated stochastic behavior in the time series for the FSRQ sources although with a large overlap between these two classes. This result indicates that the distribution of the degrees, i.e., how the flux density is distributed in time, is not the same for the light curves sources studied. So, the distribution of the degree k of the classes of light curves is not the same, and it seems that the critical exponent γ from the exponential adjustment could be useful to distinguish between these two types of blazars. On the other hand, when measuring the irreversibility of the time series with the DHVG, the distance D does not have the ability to separate the two types of blazars (Figure 5.7b).

2. In Figure 5.8a-b, we plot the critical exponent γ (UHVG) versus the square root of the normalized excess variance, and the same for parameter D (DHVG), in order to explore a possible correlation between the obtained complex networks and a variability parameter of blazars. The normalized excess variance is a quantity that indicates the observed relative strength of the variability of an astronomical source. Figure 5.8a shows a weak tendency for blazar classes, whereas the KLD and the normalized excess variance do not seem to exhibit a significant correlation in Figure 5.8b. However, as a first approach to the study of blazars with HVG, in Figure 5.8b, we managed to identify a wide range of D values among all sources (between 10^{-3} and 10^{-1} from Table 5.2) but without distinguishing between subclasses. And in Figure 5.8c, with the

bootstrap method the range of D is bounded to the order of 10^{-2}, but the KLD continues to not distinguish between subclasses. It would be convenient to calculate the γ value through the bootstrap method as well. On the other hand, it is recommended that for better comparison among sources, the normalized excess variance should be calculated using observations of the same duration [119]. This data set contains time series from 259 to 1140 data points. Therefore, even if we could truncate the light curves to match the shortest observation, this would considerably reduce our data set and analysis. However, these quantities may not be the best parameters to consider.

3. In Figures 5.9 and 5.10 we have looked for correlations with the isotropic luminosity, and also with the luminosity corrected for anisotropy and relativistic effects associated with the jet emission. However, preliminary results do not yield an apparent dependence of the complexity parameters on the luminosity of the sources. Moreover, the results of the KLD divergence through the bootstrap method shown in Figures 5.7c, 5.8c and 5.9c-f do not improve the analysis of correlations or the detection of the spectral classes of blazars with the KLD. One aspect we can report is that the scatter plot in Figure 5.9a groups most of the BL Lac sources below the limit γ_{un} at weaker isotropic radio luminosities, while the FSRQ sources are mostly above the limit at higher isotropic radio luminosities. The fact that the FSRQ sources have a higher isotropic luminosity is consistent with the blazar sequence [136].

We will continue the analysis using other tools from complex networks analysis as well as other physical parameters such as the black hole masses, radio spectral indices, or jet parameters. Although we did not find a clear correlation between γ or D with the normalized excess variance or blazar luminosities, the PDF of the critical

exponent of the degree probability distribution does show a clear difference between the two blazar classes.

6.4. Conclusions

On the whole, first, in Chapter 3 we validated the computational implementation of the Horizontal Visibility Graph algorithm on PIC simulations of magnetized plasma, where we tested with different parameters related to the velocity distributions of the particles which compose the plasma. Second, in Chapter 4 we described qualitatively the correlation between complexity parameters and solar activity, classifying between slow and fast wind during solar cycles 23 and 24 at 1 AU. And third, in Chapter 5 we found correlations with the physical characteristics of blazars.

As a final observation, the Kullback-Leibler Divergence (Equation 2.5) proved to be sensitive enough to detect differences in magnetic fluctuations of both PIC simulations and the solar wind, while the critical exponent gamma (Equation 2.4) showed some ability in distinguishing between spectral classes of blazars based on the variability of light curves in the radio band.

Other ways to analyze the complex networks and their degrees distribution $P(k)$ also can be considered. For instance, in many cases, it is useful to consider also the complementary cumulative distribution function or CDF of a variable with a power-law distribution [38, 137]. However, here, we have systematically obtained exponential distributions represented by the γ exponent. Thus, here, we have focused on the use of the HVG as a method to distinguish between slow and fast wind in the case of the solar wind, and between BL Lac and FSRQ in the case of blazars. To tackle this purpose, we have used the HVG and analyzed the distribution of the values of the γ exponent. In addition, it is known that when using the HVG, any

random series results in a network with a degree distribution of exponential type, and it has been suggested that this is a universal feature [106]. If exponential forms are not obtained, the series are related to non-randomness [15]. Nevertheless, it would be interesting to explore with the CDF to obtain perhaps a more robust statistical fitting, as discussed in the study of Zhang et al. [38].

We expect all the features observed in Chapter 3 on Kappa-distributions will provide a framework in which complex networks analysis may be used as a relevant tool to characterize turbulent plasma systems, and also as a proxy to identify the nature of electron populations in space plasmas at locations where direct in-situ measurements of particle fluxes are not available.

The results of Chapter 4 could be relevant for the understanding of the physics of the solar wind. We hope that this type of analysis, used in complex networks and systems science, can contribute to heliophysics through tools that allow data to be analyzed in new ways, even when information is limited. Our analysis could be of interest for the complementarity of physical variables that are possible to measure thanks to the progress of space exploration, but also as an approach to characterize stellar activity and stellar winds only reachable through distant observations.

Also, our results of Chapter 5 may provide some evidence for different mechanisms producing the variability in the two source spectral classes (BL Lac and FSRQ), and also open a new framework for the study of blazars, in which complex networks may be a valuable alternative tool to study AGN according to the variability of their flux density.

In closing, based on the time series associated with our systems under study, this method of constructing complex networks has delivered parameters that have characterized them in a physics-consistent manner. We have examined the intercorre-

lations responsible for the physical processes that generated the time series. We have discussed in terms of relevant systems descriptors related to dissipative characteristics, such as irreversibility, stochasticity, and complexity. Considering all of these, this thesis supports a novel study methodology for heliophysics and extragalactic astrophysics. Thus, complex networks can be a valid choice to study astronomical observations concerning the fluctuations and variability in the information presented in their time series.

Publications

The articles derived from this thesis are listed below:

1. B. Acosta-Tripailao, W. Max-Moerbeck, D. Pastén, and P. S. Moya, "Blazar light curve characterization using complex networks tools" (In preparation).

2. B. Acosta-Tripailao, D. Pastén, and P. S. Moya, "Complexity parameters of solar wind magnetic fluctuations at 1 AU during SC23 and SC24," *Astronomy & Astrophysics* (Under review).

3. B. Acosta-Tripailao, W. Max-Moerbeck, D. Pastén, and P. S. Moya, "Assigning Degrees of Stochasticity to Blazar Light Curves in the Radio Band Using Complex Networks," *Entropy*, vol. 24, no. 8, p. 1063, 2022. 10.3390/e24081063 [138]

4. B. Acosta-Tripailao, D. Pastén, and P. S. Moya, "Applying the Horizontal Visibility Graph Method to Study Irreversibility of Electromagnetic Turbulence in Non-Thermal Plasmas," *Entropy*, vol. 23, no. 4, p. 470, 2021. 10.3390/e23040470 [20]

5. B. Acosta, D. Pastén, and P. S. Moya, "Reversibility of turbulent and non-collisional plasmas: Solar wind," *Proceedings of the International Astronomical Union*, vol. 15, no. S354, pp. 363–366, 2019. 10.1017/S1743921320000137 [105]

References

[1] L. Euler, "Solutio problematis ad geometriam situs pertinentis," *Commentarii academiae scientiarum Petropolitanae*, pp. 128–140, 1741.

[2] N. Bro and M. Mendoza, "Surname affinity in Santiago, Chile: A network-based approach that uncovers urban segregation," *PLoS ONE*, vol. 16, no. 1, p. e0244372, 2021.

[3] G. Gómez Bengoechea, F. J. García Algarra, and M. L. Mouronte López, "Reducing Trade Inequality: A Network-Based Assessment," 2020.

[4] R. Ilias *et al.*, "Adaptive rewiring evolves brain-like structure in weighted networks," *Scientific Reports (Nature Publisher Group)*, vol. 10, no. 1, 2020.

[5] C. Liu, X. Wu, R. Niu, X. Wu, and R. Fan, "A new SAIR model on complex networks for analysing the 2019 novel coronavirus (COVID-19)," *Nonlinear Dynamics*, vol. 101, no. 3, pp. 1777–1787, 2020.

[6] R. Albert and A.-L. Barabási, "Statistical mechanics of complex networks," *Rev. Mod. Phys.*, vol. 74, pp. 47–97, 2002.

[7] L. Lacasa, B. Luque, F. Ballesteros, J. Luque, and J. C. Nuno, "From time series to complex networks: The visibility graph," *Proceedings of the National Academy of Sciences*, vol. 105, no. 13, pp. 4972–4975, 2008.

[8] L. Lacasa, B. Luque, J. Luque, and J. Nuño, "The visibility graph: A new method for estimating the Hurst exponent of fractional Brownian motion," *European Physical Journal*, vol. 86, p. 30001, 2009.

[9] N. Wang, D. Li, and Q. Wang, "Visibility graph analysis on quarterly macroeconomic series of China based on complex network theory," *Physica A*, vol. 391, no. 24, pp. 6543 – 6555, 2012.

[10] M. Zheng, S. Domanskyi, C. Piermarocchi, and G. I. Mias, "Visibility graph based temporal community detection with applications in biological time series," *Sci. Rep.*, vol. 11, no. 1, p. 5623, 2021.

[11] L. Telesca and M. Lovallo, "Analysis of seismic sequences by using the method of visibility graph," *Europhysics Letters*, vol. 97, no. 5, p. 50002, 2012.

[12] A. Gheibi, H. Safari, and M. Javaherian, "The Solar Flare Complex Network," *The Astrophysical Journal*, vol. 847, no. 1, pp. 115 – 127, 2017.

[13] A. Najafi, A. Hossein Darooneh, A. Gheibi, and N. Farhang, "Solar Flare Modified Complex Network," *The Astrophysical Journal*, vol. 894, no. 1, pp. 66–80, 2020.

[14] Z. Mohammadi, N. Alipour, H. Safari, and F. Zamani, "Complex network for solar protons and correlations with flares," *Journal of Geophysical Research: Space Physics*, vol. 126, no. 7, p. e2020JA028868, 2021.

[15] B. Luque, L. Lacasa, F. Ballesteros, and J. Luque, "Horizontal visibility graphs: Exact results for random time series," *Physical Review E*, vol. 80, no. 4, p. 046103, 2009.

[16] L. Lacasa and R. Toral, "Description of stochastic and chaotic series using visibility graphs," *Physical Review E*, vol. 82, p. 036120, 2010.

[17] L. Lacasa, A. Nunez, É. Roldán, J. M. Parrondo, and B. Luque, "Time series irreversibility: a visibility graph approach," *The European Physical Journal B*, vol. 85, no. 6, p. 217, 2012.

[18] L. Telesca, D. Pastén, and V. Muñoz, "Analysis of time dynamical features in intraplate versus interplate seismicity: The case study of Iquique area (Chile)," *Pure and Applied Geophysics*, vol. 177, pp. 4755–4773, 2020.

[19] V. Suyal, A. Prasad, and H. P. Singh, "Visibility-graph analysis of the solar wind velocity," *Solar Physics*, vol. 289, no. 1, pp. 379–389, 2014.

[20] B. Acosta-Tripailao, D. Pastén, and P. S. Moya, "Applying the Horizontal Visibility Graph Method to Study Irreversibility of Electromagnetic Turbulence in Non-Thermal Plasmas," *Entropy*, vol. 23, no. 4, p. 470, 2021.

[21] R. Kawai, J. M. Parrondo, and C. Van den Broeck, "Dissipation: The phase-space perspective," *Physical Review Letters*, vol. 98, no. 8, p. 080602, 2007.

[22] T. M. Cover and J. A. Thomas, "Elements of information theory second edition solutions to problems," *Internet Access*, 2006.

[23] E. Parzen, *Stochastic processes*, ser. Classics in Applied Mathematics 24. Society for Industrial and Applied Mathematics, 1999.

[24] M. L. Goldstein, D. A. Roberts, and W. Matthaeus, "Magnetohydrodynamic turbulence in the solar wind," *Annual Review of Astronomy and Astrophysics*, vol. 33, no. 1, pp. 283–325, 1995.

[25] R. Schwenn, "Solar wind sources and their variations over the solar cycle," in *Solar Dynamics and Its effects on the Heliosphere and Earth.* Springer, 2007, pp. 51–76.

[26] V. Suyal, A. Prasad, and H. P. Singh, "Hysteresis in a solar activity cycle," *Solar Physics*, vol. 276, no. 1-2, pp. 407–414, 2012.

[27] S. Redaelli and W. M. Macek, "Lyapunov exponent and entropy of the solar wind flow," *Planetary and Space Science*, vol. 49, no. 12, pp. 1211–1218, 2001.

[28] K. Gupta, A. Prasad, E. Saikia, and H. P. Singh, "Analysis of the solar wind flow during an activity cycle," *Planetary and Space Science*, vol. 56, no. 3-4, pp. 530–536, 2008.

[29] R. Blandford, D. Meier, and A. Readhead, "Relativistic Jets from Active Galactic Nuclei," *Annual Review of Astronomy and Astrophysics*, vol. 57, pp. 467–509, 2019.

[30] C. M. Urry and P. Padovani, "Unified schemes for radio-loud active galactic nuclei," *Publications of the Astronomical Society of the Pacific*, vol. 107, no. 715, p. 803, 1995.

[31] A. F. Viñas, P. S. Moya, R. Navarro, and J. A. Araneda, "The role of higher-order modes on the electromagnetic whistler-cyclotron wave fluctuations of thermal and non-thermal plasmas," *Physics of Plasmas*, vol. 21, no. 1, p. 012902, 2014.

[32] M. S. Shaw, R. W. Romani, G. Cotter, S. E. Healey, P. F. Michelson, A. C. Readhead, J. L. Richards, W. Max-Moerbeck, O. G. King, and W. J. Potter,

"Spectroscopy of Broad-line Blazars from 1LAC," *The Astrophysical Journal*, vol. 748, no. 1, p. 49, 2012.

[33] M. S. Shaw, R. W. Romani, G. Cotter, S. E. Healey, P. F. Michelson, A. C. Readhead, J. L. Richards, Max-Moerbeck, Walter, O. G. King, and W. J. Potter, "Spectroscopy of the largest ever γ-ray-selected BL Lac sample," *The Astrophysical Journal*, vol. 764, no. 2, p. 135, 2013.

[34] R. Albert and A.-L. Barabási, "Statistical mechanics of complex networks," *Rev. Mod. Phys.*, vol. 74, pp. 47–97, 2002.

[35] B. Luque, L. Lacasa, F. J. Ballesteros, and A. Robledo, "Feigenbaum graphs: a complex network perspective of chaos," *PLoS ONE*, vol. 6, no. 9, p. e22411, 2011.

[36] M. E. Newman, "Properties of highly clustered networks," *Physical Review E*, vol. 68, no. 2, p. 026121, 2003.

[37] M. G. Ravetti, L. C. Carpi, B. A. Gonçalves, A. C. Frery, and O. A. Rosso, "Distinguishing noise from chaos: objective versus subjective criteria using horizontal visibility graph," *PLoS ONE*, vol. 9, no. 9, p. e108004, 2014.

[38] R. Zhang, Y. Zou, J. Zhou, Z.-K. Gao, and S. Guan, "Visibility graph analysis for re-sampled time series from auto-regressive stochastic processes," *Communications in Nonlinear Science and Numerical Simulation*, vol. 42, pp. 396–403, 2017.

[39] É. Roldán and J. M. Parrondo, "Entropy production and Kullback-Leibler divergence between stationary trajectories of discrete systems," *Physical Review E*, vol. 85, no. 3, p. 031129, 2012.

[40] J. L. W. V. Jensen, "Sur les fonctions convexes et les inégalités entre les valeurs moyennes," *Acta mathematica*, vol. 30, no. 1, pp. 175–193, 1906.

[41] Y. Kamide and A. C. L. Chian, Eds., *Handbook of the Solar-Terrestrial Environment*. Berlin Heidelberg: Springer-Verlag, 2007.

[42] M. Yamada, R. Kulsrud, and H. Ji, "Magnetic reconnection," *Rev. Mod. Phys.*, vol. 82, pp. 603–664, Mar 2010.

[43] A. Balogh and R. A. Treumann, *Physics of Collisionless Shocks*. New York, USA: Springer-Verlag, 2013.

[44] R. Bruno and V. Carbone, "The Solar Wind as a Turbulence Laboratory," *Living Rev. Sol. Phys.*, vol. 10, no. 1, p. 2, 2013.

[45] P. H. Yoon, "Kinetic instabilities in the solar wind driven by temperature anisotropies," *Reviews of Modern Plasma Physics*, 2017.

[46] E. Marsch, "Kinetic physics of the solar corona and solar wind," *Living Rev. Solar Phys.*, vol. 3, no. 1, 2006.

[47] S. Olbert, "Summary of Experimental Results from M.I.T. Detector on IMP-1," in *Physics of the Magnetosphere*, R. L. Carovillano, J. F. McClay, and H. R. Radoski, Eds. Dordrecht: Springer Netherlands, 1968, pp. 641–659.

[48] V. M. Vasyliunas, "A survey of low-energy electrons in the evening sector of the magnetosphere with OGO 1 and OGO 3," *Journal of Geophysical Research (1896-1977)*, vol. 73, no. 9, pp. 2839–2884, 1968.

[49] M. Maksimovic, V. Pierrard, and J. Lemaire, "A kinetic model of the solar wind with Kappa distribution functions in the corona." *Astronomy and Astrophysics*, vol. 324, pp. 725–734, 1997.

[50] V. Pierrard and N. Meyer-Vernet, *Chapter 11 - Electron Distributions in Space Plasmas*. Elsevier, 2017, pp. 465–479.

[51] G. Livadiotis, M. I. Desai, and L. B. Wilson, "Generation of Kappa Distributions in Solar Wind at 1 AU," *The Astrophysical Journal*, vol. 853, no. 2, p. 142, 2018.

[52] M. Lazar, V. Pierrard, S. Poedts, and H. Fichtner, "Characteristics of solar wind suprathermal halo electrons," *Astron. Astrophys.*, vol. 642, p. A130, 2020.

[53] C. M. Espinoza, M. Stepanova, P. S. Moya, E. E. Antonova, and J. A. Valdivia, "Ion and Electron κ Distribution Functions Along the Plasma Sheet," *Geophysical Research Letters*, vol. 45, no. 13, pp. 6362–6370, 2018.

[54] A. V. Eyelade, M. Stepanova, C. M. Espinoza, and P. S. Moya, "On the Relation between Kappa Distribution functions and the Plasma Beta Parameter in the Earth's Magnetosphere: THEMIS Observations," *The Astrophysical Journal Supplement Series*, vol. 253, no. 2, p. 34, 2021.

[55] K. Dialynas, C. P. Paranicas, J. F. Carbary, M. Kane, S. M. Krimigis, and B. H. Mauk, *Chapter 12 - The Kappa-Shaped Particle Spectra in Planetary Magnetospheres*. Elsevier, 2017, pp. 481–522.

[56] C. Tsallis, "Possible generalization of Boltzmann-Gibbs statistics," *Journal of Statistical Physics*, vol. 52, no. 1, pp. 479–487, 1988.

[57] Tsallis, Constantino, *Introduction to Nonextensive Statistical Mechanics*. New York, USA: Springer-Verlag, 2009.

[58] P. H. Yoon, "Thermodynamic, Non-Extensive, or Turbulent Quasi-Equilibrium for the Space Plasma Environment," *Entropy*, vol. 21, p. 820, 2019.

[59] M. Lazar, H. Fichtner, and P. H. Yoon, "On the interpretation and applicability of κ-distributions," *Astron. Astrophys.*, 2016.

[60] A. F. Viñas, R. Gaelzer, P. S. Moya, R. Mace, and J. A. Araneda, "Chapter 7 - Linear Kinetic Waves in Plasmas Described by Kappa Distributions," in *Kappa Distributions*, G. Livadiotis, Ed. Elsevier, 2017, pp. 329 – 361.

[61] M. Lazar, R. A. López, S. M. Shaaban, S. Poedts, and H. Fichtner, "Whistler instability stimulated by the suprathermal electrons present in space plasmas," *Astrophysics and Space Science*, vol. 364, no. 10, p. 171, 2019.

[62] R. A. López, M. Lazar, S. M. Shaaban, S. Poedts, P. H. Yoon, A. F. Viñas, and P. S. Moya, "Particle-in-cell Simulations of Firehose Instability Driven by Bi-Kappa Electrons," *Astrophys. J. Lett.*, vol. 873, no. 2, p. L20, 2019.

[63] P. S. Moya, M. Lazar, and S. Poedts, "Towards a general quasi-linear approach for the instabilities of bi-Kappa plasmas. whistler instability," *Plasma Physics and Controlled Fusion*, vol. 63, p. 025011, 2020.

[64] R. E. Navarro, J. Araneda, V. Muñoz, P. S. Moya, A. F.-Viñas, and J. A. Valdivia, "Theory of electromagnetic fluctuations for magnetized multi-species plasmas," *Physics of Plasmas*, vol. 21, no. 9, p. 092902, 2014.

[65] A. F. Viñas, P. S. Moya, R. E. Navarro, J. A. Valdivia, J. A. Araneda, and V. Muñoz, "Electromagnetic fluctuations of the whistler cyclotron and firehose instabilities in a Maxwellian and Tsallis-kappa-like plasma," *J. Geophys. Res.*, vol. 120, 2015.

[66] M. Lazar, S. Kim, R. A. López, P. H. Yoon, R. Schlickeiser, and S. Poedts, "Suprathermal Spontaneous Emissions in κ-distributed Plasmas," *The Astrophysical Journal*, vol. 868, no. 2, p. L25, 2018.

[67] A. S. Sharma, M. J. Aschwanden, N. B. Crosby, A. J. Klimas, A. V. Milovanov, L. Morales, R. Sanchez, and V. Uritsky, "25 Years of Self-organized Criticality: Space and Laboratory Plasmas," *Space Science Reviews*, vol. 198, pp. 167 – 216, 2016.

[68] S. Chapman, B. Hnat, and K. Kiyani, "Solar cycle dependence of scaling in solar wind fluctuations," *Nonlin. Processes Geophys.*, vol. 15, no. 1, pp. 445 – 455, 2008.

[69] M. Domínguez, G. Nigro, V. Muñoz, and V. Carbone, "Study of the fractality of magnetized plasma using an MHD shell model driven by solar wind data," *Physics of Plasmas*, vol. 25, no. 1, p. 092302, 2018.

[70] M. Domínguez, G. Nigro, V. Muñoz, V. Carbone, and M. Riquelme, "Study of the fractality in a magnetohydrodynamic shell model forced by solar wind fluctuations," *Nonlin. Processes Geophys.*, vol. 27, no. 1, pp. 175–185, 2020.

[71] V. Muñoz, M. Domínguez, J. A. Valdivia, S. Good, G. Nigro, and V. Carbone, "Evolution of fractality in space plasmas of interest to geomagnetic activity," *Nonlin. Processes Geophys.*, vol. 25, no. 1, pp. 207–216, 2018.

[72] A. Wawrzaszek, M. Echim, and R. Bruno, "Multifractal analysis of heliospheric magnetic field fluctuations observed by Ulysses," *The Astrophysical Journal*, vol. 876, no. 1, pp. 153 – 166, 2019.

[73] T. Alberti, G. Consolini, V. Carbone, E. Yordanova, M. F. Marcucci, and P. De Michelis, "Multifractal and chaotic properties of solar wind at MHD and kinetic domains: An empirical mode decomposition approach," *Entropy*, vol. 21, no. 3, p. 320, 2019.

[74] O. W. Roberts, J. Thwaites, L. Sorriso-Valvo, R. Nakamura, and Z. Vörös, "Higher-Order Statistics in Compressive Solar Wind Plasma Turbulence: High-Resolution Density Observations From the Magnetospheric MultiScale Mission," *Frontiers in Physics*, vol. 8, p. 464, 2020.

[75] R. Chhiber, W. H. Matthaeus, T. A. Bowen, and S. D. Bale, "Subproton-scale Intermittency in Near-Sun Solar Wind Turbulence Observed by the Parker Solar Probe," *The Astrophysical Journal Letters*, vol. 911, no. 1, p. L7, 2021.

[76] S. Abe and N. Suzuki, "Complex earthquake networks: hierarchical organization and assortative mixing," *Physical Review E*, vol. 74, no. 1, p. 026113, 2006.

[77] B. Acosta, D. Pastén, and P. S. Moya, "Reversibility of Turbulent and Non-Collisional Plasmas: Solar Wind," *Proceedings of the International Astronomical Union*, vol. 15, no. S354, pp. 363–366, 2019.

[78] R. A. López, A. F. Viñas, J. A. Araneda, and P. H. Yoon, "Kinetic scale structure of low-frequency waves and fluctuations," *The Astrophysical Journal*, vol. 845, no. 1, p. 60, 2017.

[79] M. Lazar, P. H. Yoon, R. A. López, and P. S. Moya, "Electromagnetic electron cyclotron instability in the solar wind," *Journal of Geophysical Research: Space Physics*, vol. 123, no. 1, pp. 6–19, 2018.

[80] A. Wawrzaszek, M. Echim, and R. Bruno, "Multifractal analysis of heliospheric magnetic field fluctuations observed by Ulysses," *The Astrophysical Journal*, vol. 876, no. 2, p. 153, 2019.

[81] A. Balogh and L. J. Lanzerotti, "The heliosphere: Its origin and exploration," in *The Heliosphere through the Solar Activity Cycle*. Springer, 2008, pp. 1–20.

[82] R. Bruno and V. Carbone, "The solar wind as a turbulence laboratory," *Living Reviews in Solar Physics*, vol. 10, no. 1, pp. 1–208, 2013.

[83] E. Marsch and C. Tu, "Non-Gaussian probability distributions of solar wind fluctuations," vol. 12, no. 12, pp. 1127–1138, 1994.

[84] L. Sorriso-Valvo, V. Carbone, P. Veltri, G. Consolini, and R. Bruno, "Intermittency in the solar wind turbulence through probability distribution functions of fluctuations," *Geophysical Research Letters*, vol. 26, no. 13, pp. 1801–1804, 1999.

[85] L. Sorriso-Valvo, V. Carbone, P. Giuliani, P. Veltri, R. Bruno, V. Antoni, and E. Martines, "Intermittency in plasma turbulence," *Planetary and Space Science*, vol. 49, no. 12, pp. 1193–1200, 2001.

[86] L. Sorriso-Valvo, F. Carbone, E. Leonardis, C. H. Chen, J. Šafránková, and Z. Němeček, "Multifractal analysis of high resolution solar wind proton density measurements," *Advances in Space Research*, vol. 59, no. 6, pp. 1642–1651, 2017.

[87] O. W. Roberts, J. Thwaites, L. Sorriso-Valvo, R. Nakamura, and Z. Vörös, "Higher-order statistics in compressive solar wind plasma turbulence: High-resolution density observations from the magnetospheric multiscale mission," *Frontiers in Physics*, vol. 8, p. 584063, 2020.

[88] W. M. Macek and S. Redaelli, "Testing for chaos in the solar wind and Alfvénic fluctuations," *Advances in Space Research*, vol. 28, no. 5, pp. 775–780, 2001.

[89] Borovsky, Joseph Eric, "Magnetospheric plasma systems science and solar wind plasma systems science: The plasma-wave interactions of multiple particle populations," *Frontiers in Astronomy and Space Sciences*, p. 200, 2021.

[90] D. McComas, S. Bame, P. Barker, W. Feldman, J. Phillips, P. Riley, and J. Griffee, "Solar wind electron proton alpha monitor (SWEPAM) for the Advanced Composition Explorer," *The Advanced Composition Explorer Mission*, pp. 563–612, 1998.

[91] D. McComas, B. Barraclough, H. Funsten, J. Gosling, E. Santiago-Muñoz, R. Skoug, B. Goldstein, M. Neugebauer, P. Riley, and A. Balogh, "Solar wind observations over Ulysses' first full polar orbit," *Journal of Geophysical Research: Space Physics*, vol. 105, no. A5, pp. 10 419–10 433, 2000.

[92] D. McComas, H. Elliott, N. Schwadron, J. Gosling, R. Skoug, and B. Goldstein, "The three-dimensional solar wind around solar maximum," *Geophysical research letters*, vol. 30, no. 10, 2003.

[93] D. McComas, R. Ebert, H. Elliott, B. Goldstein, J. Gosling, N. Schwadron, and R. Skoug, "Weaker solar wind from the polar coronal holes and the whole Sun," *Geophysical Research Letters*, vol. 35, no. 18, 2008.

[94] I. Gnanou, C. Zoundi, W. E. Sawadogo, and F. Ouattara, "Geoeffectiveness of the inner magnetosphere under the impact of fast solar wind currents: Case of solar cycles 20 to 23," *Scientific Research and Essays*, vol. 17, no. 1, pp. 8–16, 2022.

[95] R. Hajra and J. V. Sunny, "Corotating interaction regions during solar cycle 24: A study on characteristics and geoeffectiveness," *Solar Physics*, vol. 297, no. 3, pp. 1–25, 2022.

[96] Borovsky, Joseph E, "Looking for evidence of mixing in the solar wind from 0.31 to 0.98 AU," *Journal of Geophysical Research: Space Physics*, vol. 117, no. A6, 2012.

[97] Borovsky, Joseph E., "The plasma structure of coronal hole solar wind: Origins and evolution," *Journal of Geophysical Research: Space Physics*, vol. 121, no. 6, pp. 5055–5087.

[98] R. Reda, L. Giovannelli, T. Alberti, F. Berrilli, P. Giobbi, and V. Penza, "Correlation of solar activity proxy with solar wind dynamic pressure in the last five solar cycles," 2021.

[99] S. J. Shepherd, S. I. Zharkov, and V. V. Zharkova, "Prediction of solar activity from solar background magnetic field variations in cycles 21–23," *The Astrophysical Journal*, vol. 795, no. 1, p. 46, 2014.

[100] E. Kilpua, N. Olspert, A. Grigorievskiy, M. Käpylä, E. Tanskanen, H. Miyahara, R. Kataoka, J. Pelt, and Y. Liu, "Statistical study of strong and extreme geomagnetic disturbances and solar cycle characteristics," *The Astrophysical Journal*, vol. 806, no. 2, p. 272, 2015.

[101] P. I. Reyes, V. A. Pinto, and P. S. Moya, "Geomagnetic storm occurrence and their relation with solar cycle phases," *Space Weather*, vol. 19, no. 9, p. e2021SW002766, 2021.

[102] G. de Toma, S. Gibson, B. Emery, and C. Arge, "The minimum between cycle 23 and 24: Is sunspot number the whole story?" in *SOHO-23: Understanding a Peculiar Solar Minimum*, vol. 428, 2010, p. 217.

[103] R. Lepping, M. Acũna, L. Burlaga, W. Farrell, J. Slavin, K. Schatten, F. Mariani, N. Ness, F. Neubauer, Y. Whang *et al.*, "The WIND magnetic field investigation," *Space Science Reviews*, vol. 71, no. 1, pp. 207–229, 1995.

[104] K. Ogilvie, D. Chornay, R. Fritzenreiter, F. Hunsaker, J. Keller, J. Lobell, G. Miller, J. Scudder, E. Sittler, R. Torbert *et al.*, "SWE, a comprehensive plasma instrument for the Wind spacecraft," *Space Science Reviews*, vol. 71, no. 1, pp. 55–77, 1995.

[105] B. Acosta, D. Pastén, and P. S. Moya, "Reversibility of turbulent and non-collisional plasmas: Solar wind," *Proceedings of the International Astronomical Union*, vol. 15, no. S354, pp. 363–366, 2019.

[106] V. Muñoz and N. E. Garcés, "Analysis of pulsating variable stars using the visibility graph algorithm," *PLoS ONE*, vol. 16, no. 11, p. e0259735, 2021.

[107] J. Angel and H. Stockman, "Optical and infrared polarization of active extragalactic objects," *Annual Review of Astronomy and Astrophysics*, vol. 18, no. 1, pp. 321–361, 1980.

[108] S. Vaughan, R. Edelson, R. Warwick, and P. Uttley, "On characterizing the va-

riability properties of X-ray light curves from active galaxies," *Monthly Notices of the Royal Astronomical Society*, vol. 345, no. 4, pp. 1271–1284, 2003.

[109] W. Max-Moerbeck, T. Hovatta, J. Richards, O. King, T. Pearson, A. Readhead, R. Reeves, M. Shepherd, M. Stevenson, E. Angelakis *et al.*, "Time correlation between the radio and gamma-ray activity in blazars and the production site of the gamma-ray emission," *Monthly Notices of the Royal Astronomical Society*, vol. 445, no. 1, pp. 428–436, 2014.

[110] Z. Hu and H. Tak, "Modeling Stochastic Variability in Multiband Time-series Data," *The Astronomical Journal*, vol. 160, no. 6, p. 265, 2020.

[111] M. Tarnopolski, N. Żywucka, V. Marchenko, and J. Pascual-Granado, "A comprehensive power spectral density analysis of astronomical time series. I. The Fermi-LAT gamma-ray light curves of selected blazars," *The Astrophysical Journal Supplement Series*, vol. 250, no. 1, p. 1, 2020.

[112] J. T. VanderPlas, "Understanding the Lomb–Scargle periodogram," *The Astrophysical Journal Supplement Series*, vol. 236, no. 1, p. 16, 2018.

[113] J. Kirby and C. Swain, "Power spectral estimates using two-dimensional Morlet-Fan wavelets with emphasis on the long wavelengths: jackknife errors, bandwidth resolution and orthogonality properties," *Geophysical Journal International*, vol. 194, no. 1, pp. 78–99, 2013.

[114] J. Moreno, M. S. Vogeley, G. T. Richards, and W. Yu, "Stochastic Modeling Handbook for Optical AGN Variability," *Publications of the Astronomical Society of the Pacific*, vol. 131, no. 1000, p. 063001, 2019.

[115] N. Żywucka, M. Tarnopolski, M. Böttcher, Ł. Stawarz, and V. Marchenko, "Optical variability modeling of newly identified blazar candidates behind Magellanic Clouds."

[116] L. Lacasa, B. Luque, J. Luque, and J. C. Nuno, "The visibility graph: A new method for estimating the hurst exponent of fractional Brownian motion," *Europhysics Letters*, vol. 86, no. 3, p. 30001, 2009.

[117] J. L. Richards, W. Max-Moerbeck, V. Pavlidou, O. G. King, T. J. Pearson, A. C. Readhead, R. Reeves, M. C. Shepherd, M. A. Stevenson, L. C. Weintraub *et al.*, "Blazars in the FERMI Era: The OVRO 40 m telescope monitoring program," *The Astrophysical Journal Supplement Series*, vol. 194, no. 2, p. 29, 2011.

[118] T. Hovatta and E. Lindfors, "Relativistic Jets of Blazars," *New Astronomy Reviews*, vol. 87, p. 101541, 2019.

[119] T. Turner, I. George, K. Nandra, and D. Turcan, "On X-ray variability in Seyfert galaxies," *The Astrophysical Journal*, vol. 524, no. 2, p. 667, 1999.

[120] R. Edelson, J. Krolik, and G. Pike, "Broad-band properties of the CfA Seyfert galaxies. III-Ultraviolet variability," *The Astrophysical Journal*, vol. 359, pp. 86–97, 1990.

[121] P. Rodriguez-Pascual, D. Alloin, J. Clavel, D. M. Crenshaw, K. Horne, G. A. Kriss, J. H. Krolik, M. A. Malkan, H. Netzer, P. T. O'Brien *et al.*, "Steps toward determination of the size and structure of the broad-line region in active galactic nuclei. IX. Ultraviolet observations of Fairall 9," *The Astrophysical Journal Supplement Series*, vol. 110, no. 1, p. 9, 1997.

[122] N. Aghanim, Y. Akrami, M. Ashdown, J. Aumont, C. Baccigalupi, M. Ballardini, A. Banday, R. Barreiro, N. Bartolo, S. Basak *et al.*, "Planck 2018 results-VI. Cosmological parameters," *Astronomy & Astrophysics*, vol. 641, p. A6, 2020.

[123] M. Böttcher, *Special Relativity of Jets*. John Wiley Sons, Ltd, ch. 2, pp. 17–38.

[124] T. Boutelier, G. Henri, and P.-O. Petrucci, "The influence of the jet opening angle on the appearance of relativistic jets," *Monthly Notices of the Royal Astronomical Society*, vol. 418, no. 3, pp. 1913–1922, 2011.

[125] E. Massaro, A. Maselli, C. Leto, P. Marchegiani, M. Perri, P. Giommi, and S. Piranomonte, "Multifrequency catalogue of blazars," *Multifrequency Catalogue of Blazars-5th Edition*, 2014.

[126] T. Hovatta, E. Lindfors, S. Kiehlmann, W. Max-Moerbeck, M. Hodges, I. Liodakis, A. Lähteemäki, T. Pearson, A. Readhead, R. Reeves *et al.*, "Association of IceCube neutrinos with radio sources observed at Owens Valley and Metsähovi Radio Observatories," *Astronomy & Astrophysics*, vol. 650, p. A83, 2021.

[127] Vaughan, Simon, *Scientific inference: Learning from data*. Cambridge University Press, 2013.

[128] A. B. Pushkarev, Y. Y. Kovalev, M. L. Lister, and T. Savolainen, "MOJAVE – XIV. Shapes and opening angles of AGN jets," *Monthly Notices of the Royal Astronomical Society*, vol. 468, no. 4, pp. 4992–5003, 2017.

[129] T. Hovatta, M. F. Aller, H. D. Aller, E. Clausen-Brown, D. C. Homan, Y. Y.

Kovalev, M. L. Lister, A. B. Pushkarev, and T. Savolainen, "MOJAVE: Monitoring of Jets in Active Galactic Nuclei with VLBA Experiments. XI. Spectral Distributions," *The Astronomical Journal*, 2014.

[130] D. Bryant, "Debye length in a kappa-distribution plasma," *Journal of Plasma Physics*, vol. 56, no. 1, pp. 87–93, 1996.

[131] A. Chame, "Irreversible processes: The generalized affinities within Tsallis statistics," *Physica A*, vol. 255, pp. 423 – 429, 1998.

[132] I. Gallo-Méndez and P. S. Moya, "Langevin based turbulence model and its relationship with kappa distributions," *Scientific Reports*, vol. 12, no. 1, pp. 1–8, 2022.

[133] A. Greco, W. Matthaeus, S. Perri, K. Osman, S. Servidio, M. Wan, and P. Dmitruk, "Partial variance of increments method in solar wind observations and plasma simulations," *Space Science Reviews*, vol. 214, no. 1, pp. 1–27, 2017.

[134] M. Strumik and W. M. Macek, "Testing for markovian character and modeling of intermittency in solar wind turbulence," *Phys. Rev. E*, vol. 78, p. 026414, 2008.

[135] E. Marsch and S. Liu, "Structure functions and intermittency of velocity fluctuations in the inner solar wind." in *Annales Geophysicae*, vol. 11, no. 4, 1993, pp. 227–238.

[136] E. Prandini and G. Ghisellini, "The blazar sequence and its physical understanding," *Galaxies*, vol. 10, no. 1, p. 35, 2022.

[137] A. Clauset *et al.*, "Info I709: Advanced Seminars II in Informatics: Complex Networks and Systems," *SIAM Review*, vol. 51, p. 661, 2009.

[138] B. Acosta-Tripailao, W. Max-Moerbeck, D. Pastén, and P. S. Moya, "Assigning Degrees of Stochasticity to Blazar Light Curves in the Radio Band Using Complex Networks," *Entropy*, vol. 24, no. 8, p. 1063, 2022.